Aerodynamic and heat transfer effects of distributed hemispherical roughness elements inducing step changes in a turbulent boundary layer

Olivier Léon, Philippe Reulet, François Chedevergne

Aerodynamic and heat transfer effects of distributed hemispherical roughness elements inducing step changes in a turbulent boundary layer

Olivier Léon, Philippe Reulet, François Chedevergne

ONERA/DMPE, Université de Toulouse, 2 avenue Edouard Belin, Toulouse, France

Abstract

This work details an experimental investigation aiming at characterizing aerodynamic and heat transfer effects induced by roughness elements on a fully-rough zero-pressure-gradient turbulent boundary layer (TBL). The studied rough surfaces were composed of distributed hemispherical elements in staggered arrangement over part of an otherwise flat plate, inducing step changes in roughness height and wall temperature. While the arrangement and the geometry of the roughness elements were fixed (constant density, constant plan and frontal solidities), the effect of varying the ratio of the boundary layer thickness δ to the roughness height k was investigated with a particular emphasis on low values of δ/k. In a first part of the study, mean friction coefficients and equivalent sand heights were estimated for four configurations. Quasi-wall-similarity was observed on velocity statistics, two-point correlations and spectra measured by PIV and hot-wire anemometry, suggesting that TBL large-scale structures were not significantly influenced by such large roughness elements. In a second part, heat transfer effects were investigated using mean temperature profiles and transient surface temperature measurements, highlighting discrepancies between the two approaches. Relying on the first one, a parametrization of the non-dimensional wall temperature step function was obtained, providing a semi-empirical relation for the Stanton number associated with such roughness geometries and a step change in surface temperature.

This is a post-peer-review, pre-copyedit version of an article published in International Journal of Heat and Fluid Flow. The final authenticated version is available online at: https://doi.org/10.1016/j.ijheatfluidflow.2020.108672

1. Introduction

Rough surfaces are ubiquitous in nature and in aeronautical applications, a few examples being atmospheric flows over natural terrains or urban canopies and aerodynamic flows over damaged turbine blades or iced airfoils. Compared to ideal smooth-wall situations, surface roughness generally induces increases in friction and heat transfer coefficients, but usually not in the same proportions, the ratio of these two coefficients depending on some details of the surface morphology. The key issue is then to relate the characteristics of a surface geometry to its aerodynamic and heat transfer behavior. Considering Turbulent Boundary Layers (TBLs) developing over rough surfaces, these effects translate into velocity and temperature shifts in the logarithmic region of the flow, respectively noted ΔU^+ and $\Delta\theta^+$ where the superscript $\cdot^+$ denotes inner-normalized variables. These two functions are usually unknown, even for simple "artificial", uniformly distributed geometrical roughness elements, since complex turbulent transport, 3D flow separation or elements sheltering effects prevent derivation of predictive laws from first principle. Practical models are then necessarily semi-empirical and insights in the local and homogenized effects of various roughness geometries have been mainly gained relying on experiments and fully-resolved simulations.

While the spectrum of surface roughness that exists and that should be considered for practical applications is extremely large, it is instructive to focus on the effects induced by distributed geometrical roughness elements: first, they provide precisely controlled geometrical shapes that can help isolating some mechanisms and second they may be considered as prototypes or building blocks of more natural and man-made rough surfaces such as riveted structures, iced droplets or cubical urban canopies. A significant body of work already exists on this subject and efforts aiming at experimentally characterizing the aerodynamic effects of such rough surfaces can be traced back at least to the work of Schlichting [1] who particularly investigated the effects of spheres, spherical segments, cones and tabs on the pressure losses in a channel flow. In this seminal work, Schlichting [1] also introduced the now widespread equivalent sand height, noted k_s, with reference to the former work of Nikuradse [2] who extensively studied pressure losses in pipe flows with various sizes of sieved sand grains deposited in a closely-packed manner on pipe walls. Nikuradse [2] particularly provided an empirical relationship between ΔU^+ and $k_s^+ \equiv k_s U_\tau/\nu$, where U_τ is the mean friction velocity and ν the fluid kinematic viscosity. He furthermore identified the fully-rough regime where pressure drag dominates viscous friction for $k_s^+ > 70$. This concept of equivalent sand height, acknowledged as being arbitrary by Schlichting [1], provides a reference case to compare the dynamic effect of different rough surfaces

*olivier.leon@onera.fr

in the fully rough regime and various attempts have been made in the literature to propose models or correlations yielding values of k_s given some surface morphology parameters. For example, Dirling [3], Waigh and Kind [4] and van Rij et al. [5] relied on existing experimental data obtained with various uniformly distributed geometrical roughness elements to provide empirical relationships between k_s/k and geometrical parameters such as elements spacing and element frontal, wetted and slot areas as detailed further in Sect. 2.2.

Such empirical relations are commonly employed for any type of distributed geometrical roughness element of height k, implicitly assuming that the flow developing over the studied rough surface can be considered as a TBL in the fully-rough regime. One condition for this is that the statistics and the turbulence structure of the boundary layer outside of the region of direct influence of the roughness elements (the roughness sublayer) do not depend on the surface morphology when scaled using outer velocity and length scales U_τ and δ respectively. This is known as the wall-similarity [6] or Townsend's outer-layer similarity [7] between rough- and smooth-wall TBLs. As discussed by Jimenez [8], this wall-similarity is expected to be observed only when a sufficient scale separation exists between the roughness height k and the TBL thickness δ, suggesting that a ratio $\delta/k > 40-80$ should be satisfied. There are evidence however that wall-similarity may be observed for much lower values of δ/k when dealing with 3D rough configurations. For example, Castro [9] and later Amir and Castro [10] reported wall-similarity with staggered cubes for $\delta/k > 5$ and Flack and Schultz [11] with large sand-grain roughness for $\delta/k > 16$. Such differences in thresholds are likely linked to the fact that the roughness height k is a geometric parameter that does not relevantly inform on the aerodynamic behavior of a rough surface. This led Schultz and Flack [12] to rather consider the ratio δ/k_s with values greater than 25 to ensure wall-similarity for fully-rough TBLs, thus such that $k_s^+ > 70$. Similarly, Castro et al. [13] suggested that the important parameter could be δ/z_0, where z_0 is termed the roughness length (see Sect. 2.4), with values typically greater than 300 and such that $z_0^+ > 10$ to ensure wall-similarity in a fully-rough regime. This is equivalent to $\delta/k_s > 10$ and $k_s^+ > 300$ since $z_0 = k_s \exp(-\kappa B) \approx 30 k_s$, where κ is the Kármán constant and $B \approx 8.5$. The validity of wall-similarity thus appears to depend on some details of the roughness elements considered, motivating for example the recent work of Placidi and Ganapathisubramani [14] who evaluated the impact of geometrical parameters such as frontal or planar solidities on the critical value of δ/k for large, assembled cuboid elements.

Based on this discussion dealing with the aerodynamic effects induced by geometrical roughness elements, the objective of the first part of the present work is twofold. First, most of the previous studies have focused on wall-similarity with distributed geometrical elements having cubical shapes. The present study intends to provide complementary experimental results regarding wall-similarity with distributed roughness elements having hemispherical shapes and ratios δ/k and δ/k_s smaller than the limits proposed by Schultz and Flack [12] and Castro et al. [13]. Second, the different correlations for k_s/k proposed in the literature by Dirling [3], Waigh and Kind [4] and van Rij et al. [5] are expected to be valid for hemispherical roughness configurations. Yet, significantly different estimates of k_s/k can be obtained with these correlations for a given geometry. The present work intends to provide comparative experimental results to assess the reliability of such correlations on a given configuration.

A second important aspect of the present work deals with heat transfer modifications in thermal boundary layers induced by increasingly large hemispherical roughness elements. To the knowledge of the authors, the most detailed sets of experiments investigating the effects of distributed geometrical roughness elements on thermal boundary layers were mainly conducted on two roughness geometries: packed spheres [15, 16] and staggered hemispheres [17, 18] with an arrangement similar to the one used in the present work. These two configurations were however analyzed with different objectives in mind. Pimenta et al. [15] primarily aimed at analyzing the details of momentum and heat transfers induced by a surface roughness made of packed spheres kept at constant temperature. To this end, boundary layer velocity and temperature profiles as well as Reynolds stresses and turbulent heat fluxes were measured. Building on a similar experimental setup, Ligrani and Moffat [16] explored the effects of steps in wall temperature on the characteristics of a thermal boundary layer. Here again, a detailed analysis of the structure of the TBL was conducted providing insights on the structure and development of a thermal layer inside a TBL over packed spheres. Interestingly, a direct link between $\Delta\theta^+$ and k_s^+ was proposed for this roughness geometry based on the previous work of Dipprey and Sabersky [19] (see also Ligrani et al. [20] and Kays and Crawford [21]). The sparser staggered hemispheres configuration studied by Hosni et al. [17] and Hosni et al. [18] was analyzed in a more global manner, the objective of these authors being to characterize the evolution of the Stanton number induced by such rough surfaces as a function of the Reynolds number. While characterizing such relationships is important and provided reference cases for validation of a Discrete Element Roughness Method model [22, 23], some details on the thermal boundary layer structure and the modifications of $\Delta\theta^+$ as a function of k_s^+ were not presented.

The second part of the present work intends to provide further insights on heat transfers induced by hemispherical roughness elements similar to the ones studied by Hosni et al. [17] and to highlight the differences that may exist compared to a configuration of closely-packed spheres as studied by Ligrani et al. [20]. Through these two complementary parts, a first one dealing with aerodynamic effects and a second one with heat transfer effects, it is expected to provide additional understanding of thermal TBL behavior over large distributed roughness elements.

This article is organized as follows. First, details on the experimental setup and measurement techniques aiming at characterizing TBL velocity and temperature profiles as well as friction and heat transfer coefficients on distributed hemispherical roughness elements are provided in Sect. 2. Measurement results dealing with aerodynamic effects induced by four rough

surfaces are then discussed in Sect. 3 while heat transfer coefficients and temperature profiles are analyzed in Sect. 4. Finally, conclusions on this work are summarized in Sect. 5.

2. Experimental details

2.1. Wind-tunnel and test conditions

The experiments were conducted in an Eiffel-type low-speed wind-tunnel at ONERA Toulouse, France. The cross-sectional dimensions of its working test-section are $H \times W = 300\,\mathrm{mm} \times 400\,\mathrm{mm}$ over a length of 2500 mm. Ambient air is drawn from the atmosphere into the test-section through a settling chamber (equipped with filters and honeycomb screens) and a contraction cone (having a 16:1 area contraction ratio) yielding a freestream turbulence rate measured by hot-wire anemometry (HWA) on the wind-tunnel centerline typically lower than 0.5 % for a freestream velocity of $30\,\mathrm{m\,s^{-1}}$ in the test-section.

For the present experiments, a 2 m-long smooth flat plate was mounted in the test-section with no angle of attack, as illustrated in Fig. 1. The initially laminar boundary layer developing over the upper surface was tripped using a 1 mm metal wire glued on the surface and located 180 mm downstream of the leading edge. As detailed in Sect. 3.1, the TBL obtained with this setup on a smooth surface can be considered close to "canonical" at axial locations where velocity measurements were performed, that is typically 1.3 m downstream of the wire trip. It was particularly ensured that the mean streamwise pressure gradient in the test-section was always negligible, such that $K \equiv \left(\nu/U_e^2\right)\left(\mathrm{d}U_e/\mathrm{d}x\right) < 10^{-7}$ where K is the acceleration parameter [24]. This was achieved by adjusting the angle β of the wind-tunnel roof to compensate for the growth of the TBL.

The flat plate was designed to house three consecutive plates, each one with dimensions of $360\,\mathrm{mm} \times 200\,\mathrm{mm}$ and a thickness of 10 mm. These plates may have different surface morphologies, the objective of the present work being to study rough surfaces made of distributed hemispherical elements as detailed in Sect. 2.2. The two most downstream plates of each studied configuration were uniformly heated from below, thus inducing a step change in surface temperature with respect to the first plate. As illustrated in Fig. 1, this was achieved by mounting the plates on a 10 mm-thick copper plate bonded to a heating panel. This heating panel, made of silicone and a heating electrical circuit, was regulated using a PID controller and thermocouples inserted inside the copper plates. With this setup, an almost uniform and finely controlled heating of the rough plates was achieved. In the present work, all the TBL temperature profile measurements and heat transfer estimations (see Sect. 2.5 and Sect. 2.6 respectively) were performed with a copper plate temperature regulation set to $T_c = 62\,^\circ\mathrm{C}$, typically leading to surface temperatures around 40 °C and temperature differences with respect to the external flow of about $20 \pm 5\,^\circ\mathrm{C}$. Such values yield insignificant buoyancy forces relative to inertial forces in the TBL, leading to dynamically neutral layers and allowing to consider temperature as a passive scalar of the flow. The choice of heating the two downstream plates was motivated by the need to provide sufficiently thick thermal boundary layers while keeping the complexity of the setup to a minimum (leaving the first plate unheated). The step change in surface temperature induced thus implies that the thermal boundary layer develops inside the TBL and that the two layers do not have matched thicknesses. As shown by Ligrani et al. [20] on a packed-spheres configuration, this is expected to induce alterations in temperature and turbulent heat flux profiles compared to the fully heated case. However, the logarithmic region of the mean temperature profiles and the turbulent Prandtl numbers should be relatively unaffected, two points that are of importance in the present study as detailed in Sect. 4. Finally, as shown in Fig. 1(b), the housing of the plates did not span the entire wind-tunnel test-section since a heat insulation material (PIR) was inserted inside the flat plate to reduce thermal leakage in the apparatus. This lack of roughness elements on the sides of the flat plate is not expected to bias the results obtained in this work: all the measurements were performed at mid-span and satisfactory homogeneity was observed on the mean PIV results and infrared surface temperature measurements over a span of at least 10 cm at axial locations of interest on the third rough plate.

The flow velocity U_e and temperature T_e outside of the boundary layer over the first plate were continuously monitored. All the measurements presented in this article were obtained at approximately similar aerodynamic conditions, such that $U_e = 28.5 \pm 0.5\,\mathrm{m\,s^{-1}}$ and $T_e = 20 \pm 5\,^\circ\mathrm{C}$. These aerodynamic conditions yielded friction Reynolds numbers $\delta^+ \equiv \delta U_\tau/\nu$ of about 2200 for the smooth case and approximately ranging from 3800 to 4600 for the rough cases (see Table 1). Here, δ is the TBL thickness, U_τ the estimated mean friction velocity and $\nu \approx 1.51 \times 10^{-5}\,\mathrm{m\,s^{-2}}$ the kinematic viscosity of air at the mean working temperature. The velocity was monitored using total and static pressure probes connected to calibrated differential pressure transducers (MKS Baratron) while the stagnation temperature was measured using a type K thermocouple. Note that the flow temperature varied quite significantly over the course of the measurement campaign that spanned several months due to the fact that the open wind-tunnel draws air from the external atmosphere. These temperature variations were however limited by the use of a regulated heater mounted at the air-intake of the laboratory in which the wind-tunnel is located. These air flow temperature variations were considered to be sufficiently small to induce second-order aerodynamic effects (for example, maximum variations of δ^+ lower than 4% were estimated) and were taken into account when necessary in the calibration process of the measurement devices and the post-processing of the acquired data (particularly for flow and surface temperature measurements).

Finally, one particular feature of this wind-tunnel is its transient inflow operating mode enabling the study of transient surface cooling effects and the evaluation of heat transfer coefficients following the methodology described in Sect. 2.6. This operating mode provides a setting of the flow in the wind-tunnel test-section at nominal velocity U_e with a time-scale $\tau_t \approx 1\,\mathrm{s}$ much lower than the heat transfer characteristic time-scale of the materials considered in this work (typically about 15 s based

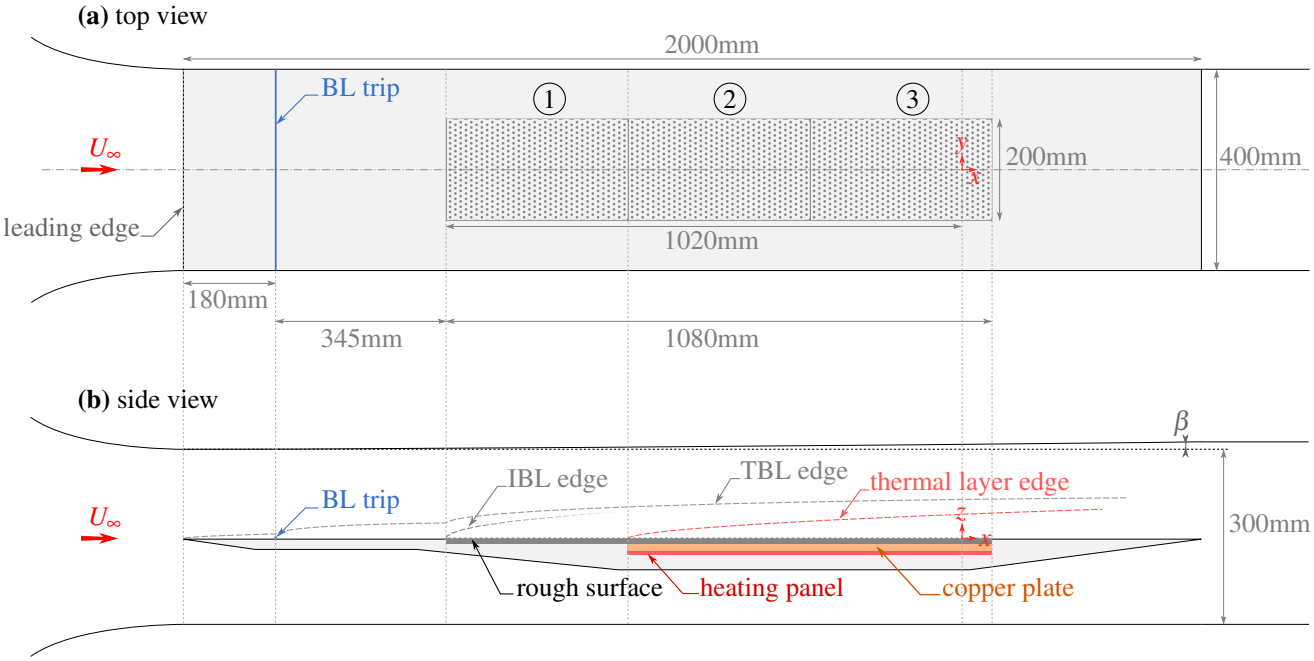

Figure 1: Schematic of the wind-tunnel test-section and the flat plate housing three identical rough plates (configuration R1 in Table 1), the last two plates being uniformly heated using a heating panel and a thick copper plate; the measurements presented in this work were obtained about 1020 mm downstream of the first row of roughness elements.

on the surface temperature transient on a smooth plate).

2.2. *Rough surface geometries and design*

The rough surfaces were made of hemispheres uniformly distributed over a flat plate in a staggered arrangement as illustrated in Fig. 2a and Fig. 2c. As displayed in Fig. 3, each hemispherical element of radius r can be viewed as being centered on an allocated square area $A_s = 16r^2$. For such geometrical elements, the upstream-facing wetted area is $A_w = \pi r^2$ and the streamwise-projected frontal area is $A_f = \pi r^2/2$. Consecutive rows of roughness elements are separated by a distance of $4r$ that is also the distance between adjacent elements in each row. This arrangement of roughness elements was chosen to be similar to the denser one found in the works of Hosni et al. [17] and Hosni et al. [18] for comparison purpose. The present staggered arrangement and density of roughness elements (around 20 %) are expected to minimize elements sheltering effects and to maximize momentum absorption.

As detailed in Table 1, four rough configurations labeled Rn with $n \in [1..4]$ were investigated. The setup R1 corresponds to roughness elements of similar height r identically distributed over the three plates, such that $r_1 = r_2 = r_3$, with r_i the radius of the elements on plate number i. The three other setups R2, R3 and R4 are characterized by increasing values of roughness heights r_2 and r_3 on the second and third plates respectively. The geometry depicted in Fig. 3 is then preserved in these cases by the application of a simple magnification factor. Considering the third plate on which all the measurements were performed, the magnification factors for cases R2, R3 and R4 relative to the configuration R1 are 1.5, 2.0 and 3.0 respectively.

These configurations were designed to induce progressive step changes in roughness conditions seen by the initially smooth-wall TBL, an objective being to obtain fully-developed TBLs over uniformly distributed roughness elements of constant k_s value on the third plate. A maximum step change $\Delta r/\delta < 8\,\%$ was observed, such that roughness element crests were always contained within the logarithmic region of the TBL. Furthermore, the length L of each plate was verified to be such that $L/\delta > 9$ for all the cases considered, a constraint that is expected to yield TBLs sufficiently adapted to the new surface morphology before sustaining another step change. This expectation is loosely derived from the work of Antonia and Luxton [26] since no clear criteria on such smooth-to-rough and rough-to-rough transitions were found by the authors. The flow velocity and temperature measurements discussed in the following sections and performed at an axial location towards the end of the third plate are thus expected to be sufficiently independent of these step changes. The results discussed in Sect. 3.3 provide support to these design choices, suggesting that each internal boundary layer induced by step changes in roughness condition have a sufficient streamwise extent to provide TBLs in near-equilibrium states. Yet, it is acknowledged that more work on this matter appears necessary but is out of the scope of the present study.

These different configurations provide cases with constant frontal and plan solidities (respectively $\lambda_f \equiv A_f/A_s = 0.1$ and $\lambda_p \equiv A_p/A_s \approx 0.2$ where $A_p = \pi r^2$ is the base surface of a roughness element), but decreasing values of $\delta/k < 30$ and increasing values of $k_s^+ > 300$ as shown in Table 1. Here, k refers to the height r_3 of the roughness elements on the third plate and k_s is the estimated equivalent sand grain height (see Sect. 2.4

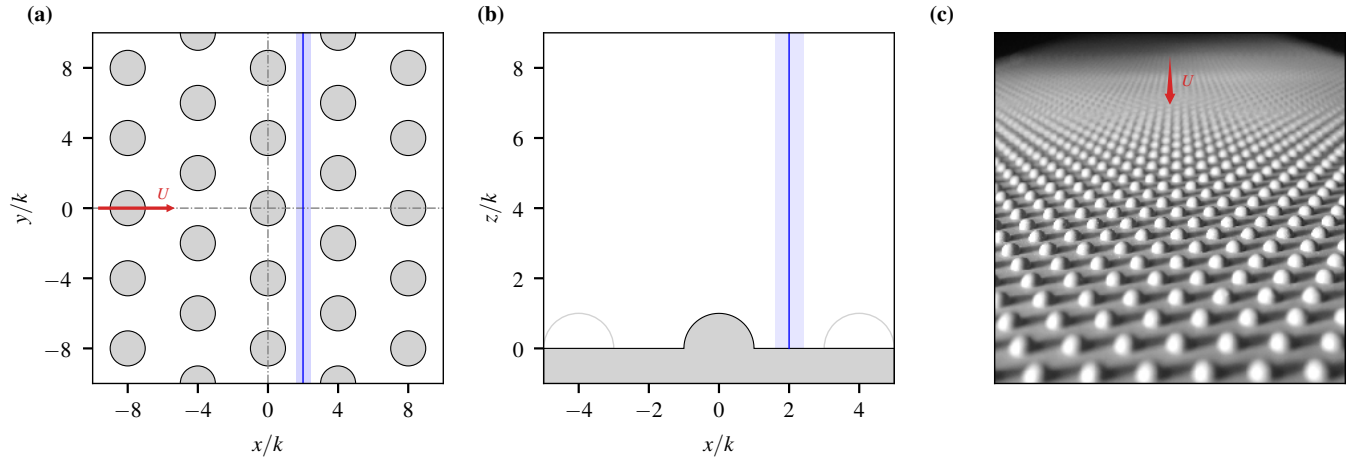

Figure 2: **(a, b)** Top and side views of the rough surface illustrating the location of the PIV measurement plane (thick blue line) and the staggered arrangement of the hemispherical elements; **(c)** Photograph of the surface R1 composed of 1.25 mm diameter staggered hemispheres in the wind-tunnel test-section.

Ref.	$k = r_3$ [mm]	r_2/k	r_1/k	δ/k	U_τ^{law} [m s^{-1}]	U_τ^{stress} [m s^{-1}]	U_τ [m s^{-1}]	$C_f/2$ $\times 10^3$	k^+	δ^+	Π	ΔU^+	z_0/k	z_0^+	k_s/k	k_s^+	e^+	e/z_0
S	0	–	–	–	1.02	–	1.02	1.3	0	2100	0.5	0	–	0	–	0	70	–
R1	1.25	1	1	29.8	1.52	1.55	1.54	2.9	130	3800	0.57	10.3	0.082	10	2.2	280	102	9.8
R2	1.875	1	0.67	21.0	1.55	1.63	1.59	3.2	200	4100	0.6	11.4	0.081	16	2.2	440	105	6.6
R3	2.5	0.75	0.5	15.4	1.67	1.70	1.69	3.5	280	4300	0.57	12.1	0.075	21	2.0	570	112	5.3
R4	3.75	0.67	0.33	10.3	1.75	1.80	1.78	4.0	440	4500	0.54	13.2	0.073	32	2.0	880	118	3.7

Table 1: Geometric and aerodynamic parameters obtained on smooth and rough wall configurations. The smooth configuration is referred to as case 'S', while rough-wall configurations are referred to as cases 'Rn' with $n \in [1..4]$. δ is the TBL layer thickness (measured from the base of the roughness elements) at which $U(\delta) = 0.995 U_e$. U_τ is the estimated friction velocity obtained by averaging the values U_τ^{law} and U_τ^{stress} given by the two estimation methods described in Sect. 2.4. C_f is the resulting estimated friction coefficient. ΔU^+ is evaluated by comparison with the log-law using the constants $\kappa = 0.39$ and $A = 4.3$. k_s is the equivalent sand grain height evaluated using $B = 8.48$ [25]. $e = 1$ mm corresponds to the estimated thickness of the PIV laser sheet and also corresponds to the approximate length of the hot-wire probe.

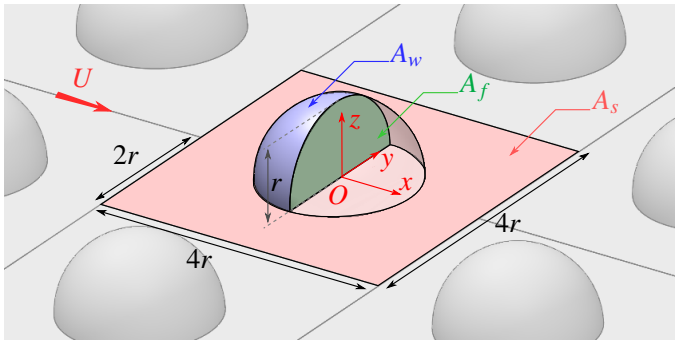

Figure 3: Geometry of the rough surfaces studied; each hemispherical element of radius r is centered on a square surface of area A_s; A_w refers to the element wetted area and A_f to the streamwise-projected frontal area; these elements are uniformly distributed in a staggered manner along the x axis.

for the details). As discussed in Sect. 1, these values of δ/k can be considered as small by the aerodynamic roughness community. It is then not clear if wall-similarity can be achieved with the present configurations, or in other words if all the cases presented are representative of TBLs developing over rough walls or if some cases should be considered as flows over a collection of obstacles. This point is investigated in Sect. 3.3.

It can also be noted that with such values of δ/k the results of this work may be considered as somewhat representative of flows over "urban" canopies made of round elements. Indeed, as shown in Table 1, the rough configurations investigated are characterized by values of $z_0^+ > 0.5$ and $z_0/k \approx 0.08$, values in agreement with the works of Cheng et al. [27] (considering an element packing density of 0.2) and Perret and Kerhervé [28] for instance. However, an important difference in the present work compared to atmospheric TBL studies lies in the smaller order of magnitude of the friction Reynolds number δ^+, implying a smaller extent of the logarithmic region, a smaller inner-outer scale separation and potentially a different activity of very large-scale structures.

Such distributed geometric roughness elements are known to induce increases in friction coefficient as their density increases, up to a point where sheltering effects start to play a significant role. This behavior leads to the identification of a sparse and a dense regime. The state of the present geometrical arrangement of roughness elements may be identified following the works of Dirling [3], Waigh and Kind [4] and van Rij et al. [5]. As mentioned in Sect. 1, these three studies derived empirical correlations for the two regimes between roughness elements geometric parameters and values of k_s/k. Since the databases considered in these works include cases with roughness elements having spherical shapes, their results

are expected to be applicable to our study.

Dirling [3] defined a dimensionless parameter Λ^*, referred to as an equivalent roughness element spacing ratio, such that

$$\Lambda^* \equiv \frac{l}{\bar{k}} \left(\frac{A_w}{A_f} \right)^{4/3}, \tag{1}$$

where l is the average roughness element spacing and $\bar{k}$ is the mean roughness elements height. For the present cases, one finds $\Lambda^* = 4(2)^{4/3} \approx 10.08 > 4.93$, a sparse regime for which elements sheltering effects are expected to decrease as Λ^* increases. The correlation proposed by Dirling [3] then yields $k_s/k \approx 139(\Lambda^*)^{-1.9} \approx 1.72$.

Waigh and Kind [4] considered a different parameter Λ measuring the effective spacing between elements and defined as

$$\Lambda \equiv \frac{A_s k}{V_r} \tag{2}$$

where $V_r = 2\pi k^3/3$ is the volume of a roughness element. For the present geometry, one obtains $\Lambda = 24/\pi \approx 7.6 > 6$ that also leads to a sparse regime — although the value obtained is close to the dense regime limit given by the authors. In this regime, Waigh and Kind [4] proposed a correlation $G(\Lambda)$ yielding $k_s/k \approx \exp(\kappa[G(\Lambda)+4]) \approx 2.37k$.

Finally, van Rij et al. [5] used a roughness parameter Λ_s defined as

$$\Lambda_s \equiv \frac{A_s}{A_f} \left(\frac{A_w}{A_f} \right)^{1.6}. \tag{3}$$

In the present case, one obtains $\Lambda_s \approx 30.9$ and the correlation proposed by van Rij et al. [5] for the sparse regime ($\Lambda_s > 28.12$) yields $k_s/k = 255.5\Lambda_s^{-1.454} \approx 1.74$, a value that is close to the one obtained using the correlation proposed by Dirling [3].

Clearly, some discrepancy exists between the estimated values of k_s/k using these three empirical correlations, despite the fact they were designed to handle such uniformly distributed simple geometric roughness elements. This might be partly explained by the fact that Dirling [3] relied on the results of Schlichting [1] that were shown to require some corrections by Coleman et al. [29]. Interestingly, van Rij et al. [5] took into account these corrections but their correlation still provides a similar estimate for the present configuration. It is not clear if these correlations are adequate for the present roughness geometry and Sect. 3 will provide experimental estimates of k_s/k for comparison and validation purpose. It is finally noted that the empirical correlation proposed by Flack and Schultz [30] and that rather considers statistical parameters of the rough surface morphology such as the r.m.s. elevation and the skewness of the surface elevation p.d.f. yields an estimate $k_s/k \approx 5.5$ that is significantly larger than the previous ones. This correlation is most likely inadequate for such sparsely distributed roughness elements and it will not be considered further in this work.

All the rough plates were made by injection molding of a polyurethane resin (Axson F19) filled with aluminum powder. This specific material was chosen for its thermal conductivity of about $0.78\,\mathrm{W\,m^{-1}\,K^{-1}}$ at $T = 60\,^\circ\mathrm{C}$, ensuring an adequate thermal diffusion time-scale to apply the transient heat transfer estimation technique described in Sect. 2.6. Prior to measurements, a sample of this resin was characterized using a dedicated facility at ONERA [31] to independently measure its thermal conductivity and specific heat for temperatures ranging from 20 °C to 70 °C.

2.3. Flow velocity measurements

The velocity statistics of the TBL developing over the rough surfaces detailed in Sect. 2.2 were measured using Particle Image Velocimetry (PIV) and Hot-Wire Anemometry (HWA). The first technique was used to investigate the statistics and spatial distribution of the three velocity components while the second one gave access to one-point one-velocity-component spectra. These measurements were also compared in Sect. 3 with two-component Laser Doppler Velocimetry (LDV) measurements performed on configurations S and R1 in a previous project [32]. These measurements being used only for comparison purpose, no details on the LDV setup are provided for conciseness. Note that all these velocity measurements were performed without heating the rough surfaces since it was verified that velocity characteristics of the TBL were not affected by the small heat transfers induced by the surface temperatures investigated.

The PIV setup designed for this experiment aimed at measuring three velocity components in (yz) planes, in-between the roughness elements as illustrated in Fig. 2a and Fig. 2b using a thick blue line. This stereo-PIV setup, mounted on a 3-axis linear stage, was composed of a double-pulse Nd:YAG PIV laser (Quantel, BSL, 200 mJ/pulse) emitting at $\lambda = 532\,\mathrm{nm}$ and two 4 MPx PIV cameras (LaVision SX4M) equipped with Scheimpflug systems and 180 mm macro lenses (Sigma). Optical 10 nm band-pass filters centered on λ were furthermore mounted on the lenses and a thin layer of rhodamine paint was applied on the rough surfaces to reduce the amount of laser light diffuse reflection at the wall observed by the cameras. The two cameras were positioned on the same side of the wind-tunnel test-section in a back-scattering configuration, the laser sheet optics being set up spanwise to avoid normal illumination of the surface. The thickness of the laser sheet e was estimated to be lower than 1 mm at mid-span. A 3D precision calibration plate (LaVision, 058-5) and a pinhole camera model accounting for optical aberrations were used to calibrate the system, yielding r.m.s. calibration errors of about 0.5 px. A measurement area with typical dimensions of $25\,\mathrm{mm} \times 40\,\mathrm{mm}$ ($\ell_z \times \ell_y$) was obtained after stereo-PIV reconstruction. Post-processing of the PIV image pairs was performed using the ONERA software FOLKI–PIV [33] using interrogation windows of 31 px, thus yielding an estimated mean spatial resolution along the vertical axis z of the order of $\Delta_z \approx 0.2\,\mathrm{mm}$. For the smooth configuration it corresponds to $\Delta_z^+ \approx 14$ and for the rough configuration R1 one gets $\Delta_z \approx 0.14k$. Note however that the actual measurement spatial resolution is most likely driven by the laser sheet thickness (the depth of field of the optical setup being slightly greater than e). Values for e^+ and e/z_0 for each configuration are given in Table 1. In the smooth case we obtained $e^+ \approx 70$, suggesting that near-wall velocity fluctuations will be significantly filtered [34]. In the rough cases, we suggest that the relevant length scale for velocity fluctuations should rather be z_0, the roughness length (see Sect. 2.4), and that the values of e/z_0 obtained

are sufficiently small to ensure satisfactory measurement of the roughness-induced fluctuations. This point is further discussed in Sect. 3. For each configuration and axial measurement location, three overlapping measurement areas were considered to cover the entire thickness δ of the TBLs. Merging of the overlapping regions was performed using a continuous polynomial blending of the mean velocity vector fields obtained and it was verified that overlapping mean and r.m.s. velocity measurements were in agreement within measurement uncertainties. A number of 2000 image pairs was acquired for near-wall measurements and was reduced to 1000 in the outer region of the TBLs.

The velocity fluctuations measured in the present highly turbulent flows were observed to be significantly larger than the random instantaneous uncertainties associated with the window-based PIV processing. This implies that the overall uncertainties on the velocity statistics are mainly driven by the number of acquired samples [35]. Estimation of these PIV measurement uncertainties was then performed relying on a bootstrap method [36] to evaluate 95% confidence intervals (CIs) on first and second moments of the velocity fields. Overall, for the most unfavorable case R4 displaying the largest velocity fluctuations, maximum 95% CIs on profiles of U, u', w', and $\langle uw \rangle$ were estimated to be $\pm 0.3\%$, $\pm 1.5\%$ $\pm 1.3\%$ and $\pm 3.7\%$ respectively. Here, capital letters refer to mean quantities, primes to r.m.s. amplitudes and angle brackets to other ensemble-averaged quantities such as velocity covariance.

HWA was performed using a boundary-layer hot-wire probe having a length of about 1.2 mm and a diameter of 5 µm (Dantec 55P15). This probe was operated in a Constant Temperature Anemometry (CTA) mode (Dantec Streamline CTA 90C10). The controller's module was configured to provide a bandwidth of about 80 kHz with an overheat ratio of 0.8. The output signal was furthermore amplified and low-pass filtered at 25 kHz to avoid aliasing (Kron-Hite analogue filter 34A), this frequency cut-off being sufficiently high to resolve the frequency content of the turbulence that was probed (see the spectra in Sect. 3). Acquisition of this signal was performed using a 24-bit acquisition module at a sampling rate of 51.2 kHz over 30 s. Calibration of this probe was performed in-situ, out of the TBL, relying on King's law and pressure measurements. Flow temperature variations mentioned in Sect. 2.1 were continuously monitored and were accounted for in data post-processing. The HWA probe was mounted on a precision linear stage (Newport UTS150PP) providing a vertical displacement accuracy of about ± 5 µm. Finally, the probe vertical location with respect to smooth and rough surfaces was estimated by placing a precision mirror of measured thickness on the surfaces (that is over the roughness elements in the rough cases) and by vertically displacing the probe down to its reflecting face. A 180 mm macro objective (Sigma) was used to accurately monitor the process, yielding accurate positioning with an estimated uncertainty of about 50 µm. The typical uncertainties associated with these HWA measurements were estimated to be around 3% for individual velocity samples with a 95% CI while reduced data such as U and u' are expected to present overall statistical uncertainties lower than 0.5% with a 95% CI.

2.4. Friction coefficient estimation

A direct measurement of the total drag acting on the roughness elements studied could not be achieved in this work for two main reasons. First, the presence of the heating panels below the rough surfaces excluded the use of floating elements. Second, the reduced size of the roughness elements precluded machining pressure taps that could have yielded an estimate of the pressure drag, the dominant drag component in the fully-rough regime. Consequently, indirect approaches were considered to estimate the mean friction drag coefficient $C_f = 2(U_\tau/U_e)^2$, where U_e is the mean axial velocity outside of the TBL and $U_\tau \equiv \sqrt{\tau_w/\rho}$ is the mean friction velocity deduced from the total mean shear stress τ_w acting on the surface. It is acknowledged that such indirect approaches necessarily suffer from some defects and as a consequence two different methods were used.

The first method relies on a semi-empirical analytic representation of the mean axial velocity profile $U(z)$ of a zero-pressure-gradient TBL over rough walls valid above the roughness sublayer. This profile $U_{\text{law}}(z)$ made dimensionless using U_τ is defined as

$$U^+_{\text{law}}(z) \equiv U^+_{\log}(z) + \frac{2\Pi}{\kappa}\omega(\eta) \tag{4}$$

$$U^+_{\log}(z) \equiv \frac{1}{\kappa}\log(z-\varepsilon)^+ + A - \Delta U^+, \tag{5}$$

where κ is the Kármán constant, ε is the vertical shift of origin induced by the presence of roughness elements (with z measured from the base of the roughness elements as shown in Fig. 2(b); this parameter must satisfy $0 \leq \varepsilon \leq k$), A is the smooth-wall intercept constant, ΔU^+ is the (Hama) roughness function, Π is the wake parameter and $\omega(\eta)$ is the law of the wake that is a function of $\eta \equiv (z-\varepsilon)/\delta < 1$. While some debate exists in the literature regarding the universality and the exact values of κ and A to consider in zero-pressure-gradient TBL over smooth and rough walls [37], we chose to set $\kappa = 0.39$ and $A = 4.3$ as in the works of Squire et al. [38] and Nagib and Chauhan [39]. Furthermore, various forms of the law of the wake $\omega(\eta)$ were proposed in the literature for TBL over smooth surfaces. These wake functions have been commonly assumed to present some degree of universality and thus to be valid for TBLs over rough surfaces (see for example Castro [9]). To be consistent with our previous choice of κ and A, we selected the wake function proposed by Chauhan et al. [40].

Fitting Eq. (4) to the measurement data leads to an optimization problem with 4 parameters (U_τ, ε, ΔU^+ and Π), assuming known values for κ, A and δ. This was performed by minimizing a mean-square-difference cost function evaluated from the spanwise averaged mean axial velocity profiles measured by PIV and Eq. (4) for the grid points typically satisfying $z-k > 0.05(\delta-k)$, that is for measurements approximately out of the region of influence of the roughness elements as observed in Fig. 8(a) and Fig. 8(b) for instance. Two main issues were identified with this approach. First, the boundary layer thickness δ is usually defined in the law of the wake as the theoretical value for which $U(\delta) = U_e$ exactly. Its value can then be quite different from $\delta_{99.5}$, the boundary layer thickness for which

$U(\delta_{99.5}) = 0.995U_e$ that is commonly used when dealing with experimental results. This approximation was observed to introduce a significant additional source of uncertainty in the estimation of C_f which was alleviated by leaving δ as an additional free parameter. Second, a strong coupling between ε and the other parameters was observed, suggesting that this parameter cannot be estimated in a robust and accurate manner relying on such approach with the present measurements. Alternatively, a single constant value for ε was first estimated relying on the following rationale. First, ε is not expected to vary for a given roughness geometry in the fully-rough regime as discussed by Raupach et al. [6]. As a consequence, if all the present rough cases could be considered as TBLs in a fully-rough regime (that is if wall-similarity is observed), ε/k should be invariant. Second, the application of the estimation method of ε proposed by Perry and Li [41] yielded similar values for all the cases here considered, a mean value of $\varepsilon/k \approx 0.3 \pm 0.1$ being obtained. Such a value appears physically acceptable since typical estimates for cubical roughness elements distributed with similar density and arrangement are close to 0.6 [28], a value that is expected to be higher than with spherical elements where the projected frontal section is comparatively reduced towards the elements crest. We finally mention that an other common way of estimating ε in the literature is found in the work of Jackson [42] who proposed to interpret ε as the wall-coordinate where the average surface drag is acting. Relying on a roughness-resolved RANS simulation conducted on a case similar to configuration R1 (performed and validated in the course of an other project by the authors and not discussed here for conciseness) an estimated value of $\varepsilon/k \approx 0.44$ was obtained, slightly larger than the previous estimate. This difference may be explained by the works of Cheng et al. [27] and Loureiro and Freire [43] who proposed that these two estimates obtained following Perry and Li [41] and Jackson [42] may not be equivalent. Relying only on experimental data for the present work, ε/k was set to 0.3 and the final optimization parameters left were (U_τ, ΔU^+, δ, Π). Note however that setting $\varepsilon/k = 0.4$ yields comparable results with values of U_τ generally lower by about 2%.

It can be mentioned at this point that the law given by Eq. (4) can be written in a velocity-defect form, as used for example by Krogstad et al. [44], decrementing the number of unknowns by eliminating $A - \Delta U^+$ and introducing the measured mean external velocity U_e. No significant improvements on the values of the optimized parameters were however observed using this formulation. We further note that an alternative way of writing Eq. (5) is usually preferred in the meteorological community, such that

$$U^+_{\log}(z) = \frac{1}{\kappa} \log\left(\frac{z-\varepsilon}{z_0}\right). \tag{6}$$

The roughness length z_0 embeds the aerodynamic roughness effects and is then directly linked to the roughness function ΔU^+, thus leaving the number of free parameters unchanged.

The second method used to estimate C_f relies on the concept of equilibrium layer where approximate constant stress is expected [6]. While this is well verified in smooth-wall TBLs, it can also be expected to be observed in rough-wall TBLs assuming wall-similarity. Considering the streamwise momentum equation of a zero-pressure-gradient TBL and neglecting viscous terms and axial derivatives in this layer yields

$$\frac{C_f}{2} \approx \frac{-\langle uw \rangle_{z_I}}{U_e^2} \tag{7}$$

where $-\langle uw \rangle$ is the mean Reynolds stress and z_I a vertical position (above the roughness crests) inside the constant-stress layer, that is approximately equivalent to the inner, inertial layer. Here, we will consider the maximum value of $-\langle uw \rangle$ reached above the roughness height. Such an approach was used for example by Krogstad et al. [44] or Ligrani and Moffat [25], the latter authors stating that the terms neglected in the momentum equation contributed to about 2 to 4% of the total shear stress in their cases of study. The main advantage of this technique is that the estimation of C_f does not depend on ε. It relies nonetheless on some assumptions and precise measurements of Reynolds stresses. Estimates of C_f are then usually expected to be accurate at $\pm 5\,\%$. One may note however that Cheng et al. [27] reported potential errors using this approach of the order of 25 % on values of C_f while studying TBLs over large cubical roughness elements ($\delta/k \approx 6$). Yet, in the present work, a satisfactory agreement was observed between values of C_f obtained using the two detailed methods (see Sect. 3), suggesting that the error may not be that large for the present cases of study.

These two approaches were applied on spanwise-averaged PIV measurements providing two friction velocity estimates for each case, referred to as U_τ^{law} and U_τ^{stress} in Table 1. The final friction velocity estimate U_τ was then obtained by averaging these two values.

2.5. *Flow and surface temperature measurements*

Thermal boundary layer mean temperature profiles were measured using a constant-current cold-wire thermometer (1 µm diameter platinum wire, Dantec 55P31) operated at a constant current of 0.1 mA to ensure negligible sensitivity to velocity. Calibration of this probe over a range of temperature from 20 °C to 60 °C was performed using a dedicated setup composed of a small-size jet regulated in both temperature and mass-flow-rate and a reference PT100 probe. The output signal of the module was low-pass filtered at 3 kHz and acquired at a rate of 6 kHz over 30 s. Vertical displacements and positioning of this probe in the wind-tunnel section were performed using the same procedure and apparatus described in Sect. 2.3 for HWA, yielding similar positional uncertainties. We furthermore estimated that the typical mean temperature measurement uncertainty associated with the apparatus and the calibration process should be around $\pm 0.5\,^\circ$C over the range of temperature explored.

Surface temperature measurements were performed on the third plate of each configuration using infrared (IR) thermography. This was achieved using an infrared camera (FLIR SC7650 MWIR) equipped with a 640 px × 512 px temperature-regulated sensor and a dedicated 25 mm lens. A ZnSe window

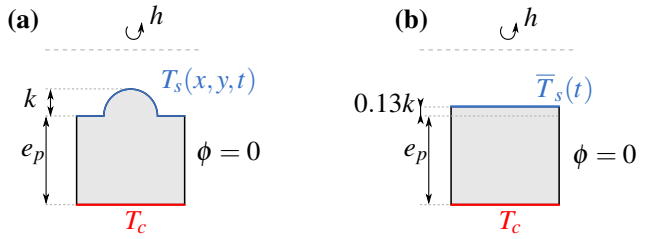

Figure 4: Modeling assumption used to estimate the heat transfer coefficient h of a rough surface using transient surface temperature measurements $T_s(x,y,t)$. **(a)** represents a pattern of the real rough surface while **(b)** illustrates the simplified "melt-down" case on which a spatial-averaged transient surface temperature $\overline{T}_s(t)$ is considered. The sides are assumed adiabatic ($\phi = 0$).

having a measured transmissivity $\tau = 0.96 \pm 0.01$ for wavelengths ranging from 3 µm to 5 µm was mounted in the wind-tunnel ceiling above the region of interest. A measurement area of 194 mm × 155 mm was obtained with a spatial resolution of 0.3 mm/px approximately. Finally, considering only the transmittance of the infrared translucent window, the radiation I_c measured by the IR camera was assumed to be given by

$$I_c(T_w, T_e) = \varepsilon_s \tau I(T_w) + (1 - \varepsilon_s \tau) I(T_e) \tag{8}$$

where $I(T_w)$ is the radiation from the test surface at temperature T_w, $I(T_e)$ is the radiation from the surrounding that is assumed to be at the flow temperature T_e (thus accounting for radiation from the wind-tunnel walls) and $\varepsilon_s = 0.92 \pm 0.02$ is the estimated emissivity of the surface over the wavelength bandwidth of the camera. Measurements were performed over a duration of 60 s for both transient and stationary wind-tunnel conditions at an acquisition rate of 10 Hz and with an integration time of 1.2 ms. Given the measurement uncertainty of ±1 °C given by the camera manufacturer and our estimated uncertainties on τ and ε_s, an overall uncertainty on T_w was evaluated to be around 1.5% over the range of surface temperature explored.

2.6. Heat transfer coefficient estimation

The mean heat transfer coefficient h associated with each rough configuration was estimated relying on two methods. The first one is based on a transient thermal analysis using surface temperature measurements obtained by IR thermography. This technique was selected over the classical energy balance approach to avoid estimating heat losses and to obtain local estimates rather than global ones. First, the two downstream plates were heated without flow in the test-section. Then, using the rapid transient mode of the wind-tunnel, a stationary flow was set in the test-section. IR thermography acquisitions were started 5 s before the transient and lasted 60 s, a duration that was observed to be sufficient to provide satisfactory estimates of h. In a last step, the spatio-temporal surface temperature measurements $T_s(x,y,t)$ were applied as boundary conditions in an in-house unsteady heat conduction solver where the rough surface was modeled considering adiabatic side walls to account for the periodic arrangement of elements and a uniform constant temperature T_c on the lower face. To be accurate, one needs to consider a 3D unsteady conduction problem as illustrated in Fig. 4(a), taking into account the roughness geometry. Solving this problem was however observed to yield questionable local results near the roughness element likely due to a poor spatial resolution in surface temperature measurement and significant temperature uncertainties on the sides of the hemispheres, the IR camera optical axis being oriented almost vertically. As a consequence, we rather considered the approximate 1D problem illustrated in Fig. 4(b). The measured surface temperature $T_s(x,y,t)$ was spatially averaged over a few roughness elements around the axial location of interest to yield $\overline{T}_s(t)$ that served as a spatially-uniform temporal boundary condition on a smooth surface. This approximation has previously been used by Bons [45] for example to estimate heat transfer coefficients on rough surfaces. Note here that the added volume introduced by the hemispheres was accounted for by adding a $0.13k$ thick layer as a simple "melt-down" approximation. Solving this problem provided a spatially-averaged transient heat flux estimate $\overline{\phi}(t)$ at the fluid-solid interface and the associated heat transfer coefficient $\overline{h}(t)$ was evaluated by accounting for radiation heat transfer losses as

$$\overline{h}(t) = \frac{\overline{\phi}(t) - \varepsilon_s \sigma \left(\overline{T}_s(t)^4 - T_e(t)^4 \right)}{\overline{T}_s(t) - T_e(t)} \tag{9}$$

where T_e is the flow temperature outside of the TBL. The final mean heat transfer coefficient h was then obtained by averaging $\overline{h}(t)$ over 50 s after a short initial transient, a duration over which quasi-steady values were observed. The total uncertainty on h associated with this estimation approach is quite difficult to assess as the main hypothesis used, namely the equivalence between exact 3D and averaged 1D conduction problems, cannot be easily estimated without conducting a dedicated numerical investigation that is out of the scope of the present experimental work. Nonetheless, since such a simplified approach has already been apparently successfully employed in the literature in a similar context, it is of interest to evaluate its relevance for the present rough configurations. We furthermore note that an uncertainty of at least 5% induced by the estimated properties of the material used should be considered.

The second technique used to estimate mean values of h relies on mean temperature profiles $T(z)$ measured by cold-wire thermometry. Indeed, similarly to mean velocity profiles, mean temperature profiles $T(z)$ for thermal layers developing inside a TBL display a logarithmic region, as shown by Ligrani and Moffat [25] for instance, that can be written as

$$\frac{T(z) - T_e}{T_\tau} = -\frac{1}{\kappa_\theta} \log \frac{z - \varepsilon_T}{\delta_T} + D_\theta \tag{10}$$

using external temperature and length scales. Here, T_e is the external mean temperature, T_τ is the friction temperature, κ_θ is identified as κ/Pr_t with Pr_t the turbulent Prandtl number, δ_T is the thermal boundary layer thickness, ε_T is the zero-plane vertical displacement of the thermal boundary layer and D_θ is the log-law intercept. As discussed by Loureiro and Freire [43], we note here that the wall correction parameter for the temperature ε_T should be different from ε, the wall correction parameter for the velocity log-law. Relying on an approach similar

to the one proposed by Perry and Li [41] for velocity profiles, estimates for ε_T were evaluated for each rough configuration yielding $0 < \varepsilon_T < 0.1k$.

Assuming a constant value for κ_θ, fitting this relation on the measured temperature profiles provides estimates for T_τ. Here, we considered $\kappa_\theta = 0.39/0.82 \approx 0.48$, a value that is close to the value 0.47 proposed by Kader [46] and similar to the one used by Perry and Hoffmann [47] for smooth-wall thermal turbulent boundary layers. The friction temperature is furthermore defined as

$$T_\tau \equiv \frac{\Phi}{\rho c_p U_\tau} \tag{11}$$

where Φ is the mean heat flux and ρ and c_p are the density and heat capacity of air at T_e. The mean heat transfer coefficient h is then obtained by

$$h \equiv \frac{\Phi}{(T_w - T_e)} = \frac{\rho c_p T_\tau U_\tau}{T_w - T_e} \tag{12}$$

where T_w is the mean wall temperature that was estimated using IR thermography measurements acquired in a steady state. The total uncertainty associated with such estimates of h then mainly depends on the uncertainties on T_τ, U_τ and T_w, that are respectively about 5%, 5% and 1.5% with a 95% CI. Consequently, propagation of uncertainties leads to a global uncertainty on h of about 7%. The Stanton number is finally defined as

$$\mathrm{St} \equiv \frac{h}{\rho c_p U_e} = \frac{T_\tau}{T_w - T_e}\frac{U_\tau}{U_e} \tag{13}$$

where U_e is the mean external velocity.

3. Aerodynamic results

3.1. Smooth flat plate

Before discussing the aerodynamic results obtained over rough surfaces, a validation of our experimental setups on a smooth-wall TBL is presented. Velocity statistics measured by PIV and HWA are displayed in Fig. 5, showing profiles of mean axial velocity $U^+ \equiv U/U_\tau$, axial velocity r.m.s. amplitude $u'^+ \equiv u'/U_\tau$ and Reynolds stress $-\langle uw\rangle^+ \equiv -\langle uw\rangle/U_\tau^2$. At the measurement axial location that is about 1.3 m downstream of the tripping device, the TBL is characterized by displacement and momentum thickness Reynolds numbers $\mathrm{Re}_{\delta_1} \approx 8500$ and $\mathrm{Re}_\theta \approx 6200$ respectively. Other TBL parameters may be found in Table 1. The estimated mean friction velocity $U_\tau \approx 1.05\,\mathrm{m\,s^{-1}}$ used to make the profiles dimensionless was evaluated relying on a fit to the PIV data of the composite velocity profile proposed by Chauhan et al. [40]. Note that the PIV profiles presented are the result of ensemble and spanwise averages whereas HWA results were acquired at a single mid-span location. An excellent agreement between PIV data, HWA data and the composite profile can be observed over the entire boundary layer thickness. Additional measurements obtained using LDV are overlayed, displaying again a satisfactory collapse. Note that the first valid data point obtained by PIV is

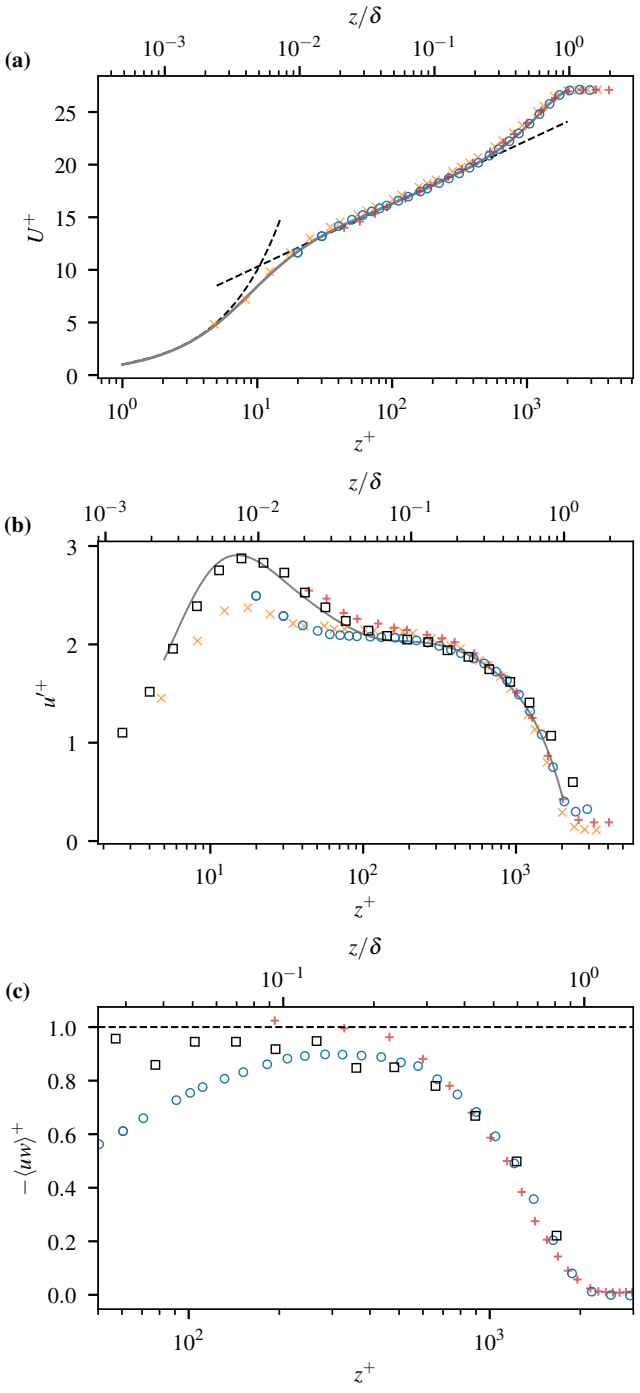

Figure 5: Vertical profiles of velocity statitics measured in a TBL using PIV (○), HWA (×) and LDV (+) on a smooth flat plate for $\delta^+ = 2100$, where δ is the TBL thickness for which $U = 0.995U_e$, and $\mathrm{Re}_\theta \approx 6200$. Are also shown the LDV measurements (□) reported by De Graaff and Eaton [24] in a TBL at $\mathrm{Re}_\theta = 5200$. **(a)** Mean axial velocity profiles $U^+ \equiv U/U_\tau$ with U_τ evaluated using a fit on the PIV data of a composite profile (——) developed by Chauhan et al. [40]; are also displayed using dashed lines (- - -) the two functions $U^+ = z^+$ and $U^+ = 1/\kappa \log(z^+) + A$ with the values of κ and A proposed in [40]. **(b)** R.m.s. axial velocity profiles u'^+ compared with the semi-empirical profile (——) proposed by Marusic and Kunkel [48]. **(c)** Reynolds stress $-\langle uw\rangle^+$ profiles obtained with 2C LDV and 3C PIV.

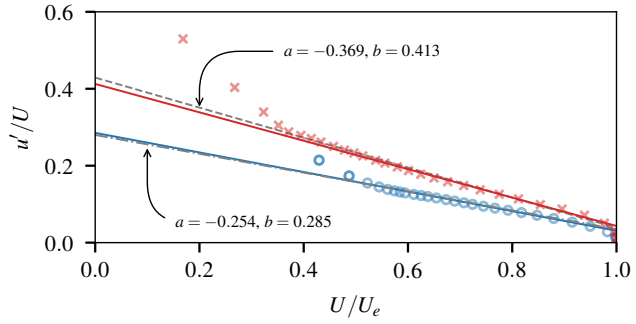

Figure 6: Diagnostic plots deduced from PIV measurements and obtained for the cases S (○) and R1 (×); the linear regressions proposed by Alfredsson et al. [49] and Castro et al. [13] for smooth and fully-rough TBL are displayed using solid colored lines; linear regressions $aU/U_e + b$ of our data were evaluated on a range $0.7 < U/U_e < 0.9$ and are shown using dashed gray lines.

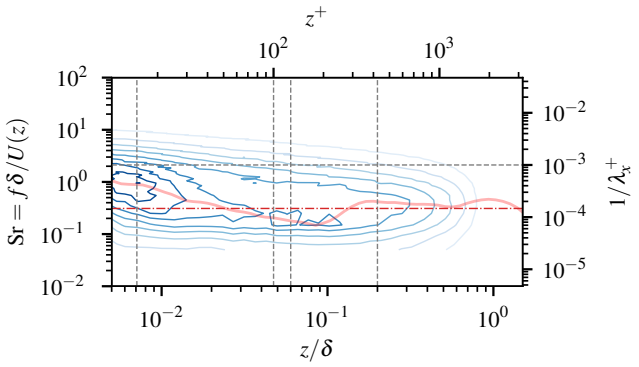

Figure 7: Pre-Multiplied spectral map $fS_{uu}(z,f)/U_\tau^2$ obtained by HWA on a smooth flat plate at $\delta^+ \approx 2100$. The ridge of maximum intensity is displayed using a thick red line (——). The dashdot red line (-·-·-) indicates $\mathrm{Sr} = 0.3$. The vertical dashed gray lines (- - -) indicate $z^+ = 15$, $z^+ = 100$, $z/\delta = 0.06$ and $z/\delta = 0.2$ respectively.

located at $z^+ \approx 20$ in agreement with the value of Δz^+ given in Sect. 2.3 while HWA provided a first valid point at $z^+ \approx 5$.

The fit of the composite profile gave a value for the wake parameter $\Pi \approx 0.52$ that is 18 % higher than the value 0.44 proposed by Chauhan et al. [40] for "canonical" zero-pressure-gradient TBL. The estimated shape factor $H \approx 1.39$ is nonetheless only 2 % higher than the expected value of 1.36 at $\mathrm{Re}_{\delta_1} = 8500$ [40]. This suggests that the present TBL does not present the exact characteristics recommended by Chauhan et al. [40] to be considered as "well-behaved", which may be expected due to the reduced available development length of the TBL. We consider nonetheless that this smooth-wall TBL provides sufficiently adequate statistics to serve as a reference case for the present study that mainly discusses large roughness effects. This is particularly supported by the use of the diagnostic plot $u'/U = f(U/U_e)$ proposed by Alfredsson and Örlü [50] and shown in Fig. 6 for the two cases S and R1. An excellent agreement is found between the present smooth-wall data and the linear regression proposed by Alfredsson et al. [49] for "well-behaved" smooth-wall TBLs.

Regarding the axial velocity fluctuation amplitudes u'^+, a satisfactory agreement is obtained between PIV, HWA and LDV in Fig. 5b for $z^+ > 100$. These measurements also compare favorably with the semi-empirical law proposed by Marusic and Kunkel [48] and the LDV measurements reported by De Graaff and Eaton [24] for $\mathrm{Re}_\theta = 5200$, validating the measurements in this region. For $z^+ < 100$ however, PIV and HWA measurements clearly show a similar under-estimation of r.m.s. velocity amplitudes. This is attributed to spatial filtering effects [34] induced by the PIV laser sheet thickness and the hot-wire length, both having similar values. It is furthermore observed in Fig. 5c that the Reynolds stress $-\langle uw \rangle^+$ measured by PIV compares very favorably with our LDV results and with the measurements reported by De Graaff and Eaton [24] for $z^+ > 200$, with an apparent slight under-estimation of the maximum value that is likely the consequence of the previously mentioned spatial filtering effects.

It is finally instructive to examine the pre-multiplied axial velocity spectra $fS_{uu}(z,f)/U_\tau^2$ in logarithmic scales deduced from HWA measurements and shown in Fig. 7. This spectral map displays a peak in the inner region of the TBL, located at $z^+ \approx 20$ and at a Strouhal number $\mathrm{Sr} \equiv f\delta/U(z) \approx 0.85$. Relying on Taylor's hypothesis of frozen turbulence usually applied in such a context, this Strouhal number is approximately equivalent to $\lambda_x^+ \approx 2000$ where λ_x is a streamwise wavelength. These values are different from $z^+ \approx 15$ and $\lambda_x^+ \approx 1000$ reported in the work of Hutchins and Marusic [51], a discrepancy that could be explained by near-wall spatial filtering effects previously discussed. Nonetheless, more importantly for the present work, one can observe that the spectral ridge displayed using a thick red line fluctuates around a value of Strouhal number $\mathrm{Sr} \approx 0.3$ in both the logarithmic and the outer layers (that is for $z^+ > 200$), which is equivalent to $\lambda_x/\delta = 1/\mathrm{Sr} \approx 3$. This value is in agreement with the measurements discussed by Mathis et al. [52] for instance and is generally identified as the signature of large-scale coherent structures (LSS). Finally, as in the work of Hutchins and Marusic [51] at approximately matched δ^+, a slight indication of the appearance of an outer-peak at $z/\delta \approx 0.06$ can be observed. These results thus suggest that the outer-region frequency content of the present smooth-wall TBL is comparable with established results in the literature.

These comparisons show that the present experimental setups and data processing provide satisfactory measurements in the logarithmic and wake regions of a smooth-wall TBL but may yield spatially-filtered data in the near-wall region where small-scale eddies drive the flow fluctuations. Since this work mainly addresses the effects of roughness elements where relevant length scales will be larger, this limitation can be tolerated as shown in Sect. 3.2.

3.2. *Influence of hemispherical roughness elements on TBL velocity statistics*

The effects induced by distributed hemispherical elements on TBL velocity statistics are now discussed in comparison with the previously described smooth-wall TBL. To this end, only

the first rough surface R1 is considered here in details, the effect of varying δ/k being discussed in Sect. 3.3.

Profiles measured by PIV, HWA and LDV on configuration R1 are shown in Fig. 8. These profiles were obtained at similar axial locations, between two consecutive rows of roughness elements such that $x = 2k$. Note again however that HWA and LDV profiles were obtained at a specific spanwise location, behind one roughness element at $y = 0$, while PIV profiles are the result of a spanwise-averaging operation over $\ell_y = 40\,\text{mm}$, yielding different results in the roughness sublayer. As observed in Fig. 8a displaying mean axial velocity profiles U/U_e, a satisfactory agreement is obtained between the different measurement techniques in the entire TBL. Out of the roughness sublayer, here typically for $z > 2k$, a good agreement is also obtained on the r.m.s. axial velocity profiles u'/U_e shown in Fig. 8b. PIV measurements performed at 3 upstream axial locations using 50 mm displacement steps are also depicted using blue solid lines, illustrating the streamwise consistency of the measurements in this configuration and the low dispersion obtained on the statistics here discussed. These results support the relevance of PIV and HWA in accurately measuring velocity fluctuations in such rough configurations where the length-scales of energy-containing eddies are expected to be larger compared to the smooth-wall configuration as mentioned in Sect. 2.3. One may particularly observe that local PIV (dashed purple line) and HWA results (orange circles) are able to correctly capture the peak in u' at $z = k$ measured by LDV. The discrepancies observed below the roughness crest ($z < k$) are likely the result of limitations on each measurement technique in this region: one may mention for instance spatial resolution effects for PIV, near-wall light scattering effects for LDV and large 3D flow effects for single-wire HWA. The relevance of the PIV measurements is further supported by Fig. 8c giving the Reynolds stress profiles measured by LDV and PIV, both providing similar results out of the roughness sublayer and a similar estimate of the friction coefficient at the outer edge of the logarithmic region, such that $C_f^{\text{stress}} \approx 0.003$ following Eq. (7). As discussed in Sect. 2.4, a second estimated value of C_f was obtained using a fit of a composite mean velocity profile, yielding $C_f^{\text{law}} \approx 0.0028$. Corresponding values of U_τ are reported in Table 1. A satisfactory agreement is thus obtained relying on these two approaches, with relative differences of about 3% compared to the mean estimate $C_f = 0.0029$. Note that similar agreements were observed for the three other rough configurations listed in Table 1.

Estimating U_τ from this value of C_f, the roughness function ΔU^+ was evaluated by estimating the mean difference in the logarithmic region of the flow between the measured profile $U^+(z^+)$ and the smooth-wall reference law given by Eq. (5). The equivalent sand grain height k_s may then be obtained by applying the relation proposed by Nikuradse [2] for rough pipes flows that reads

$$\Delta U^+ = \frac{1}{\kappa^*} \log k_s^+ + A^* - B \tag{14}$$

with $\kappa^* = 0.4$, $A^* = 5.5$ and $B = 8.48$. We may argue however, as in the work of Ligrani and Moffat [25], that the values

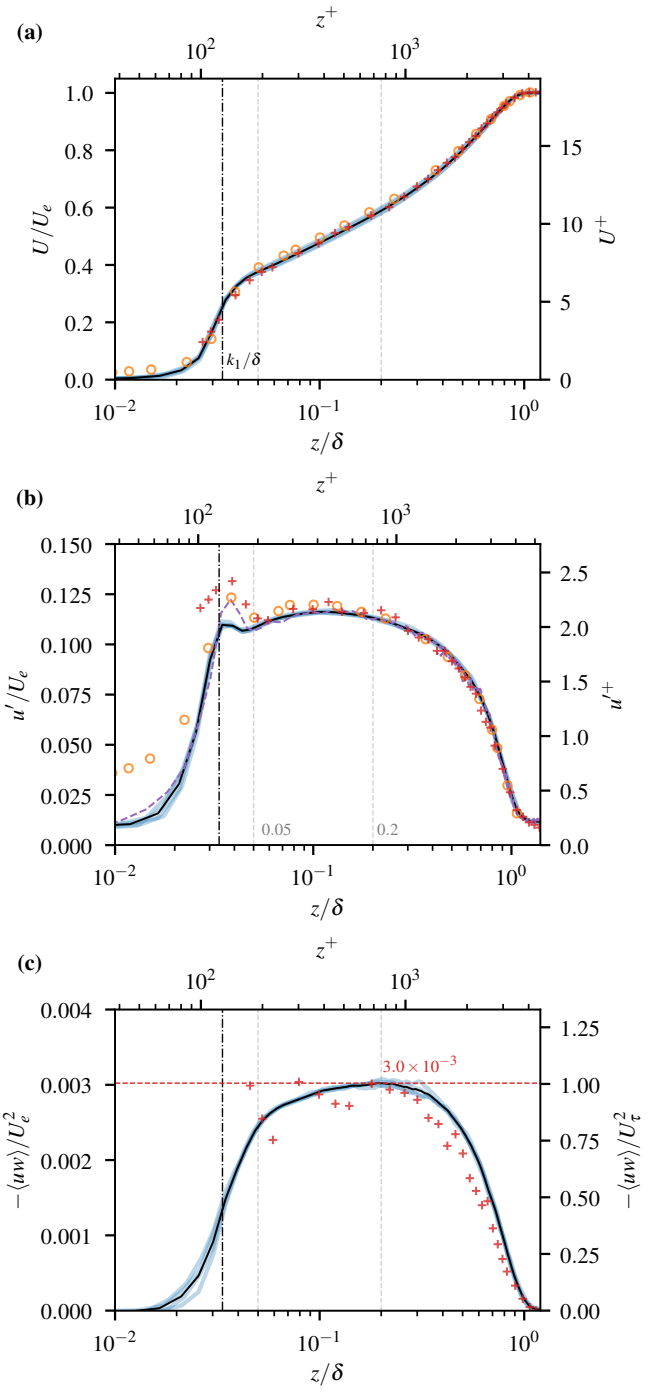

Figure 8: Profiles of **(a)** mean axial velocity, **(b)** axial velocity r.m.s. amplitude and **(c)** Reynolds stress measured by stereo-PIV (spanwise-averaged results: ——; local profile at $y = 0$: - - -), HWA (○) and LDV (+) obtained on configuration R1. Profiles measured by PIV at upstream axial locations in-between rows of roughness elements are shown using thin blue solid lines (——). The vertical black dashdot lines (-·-·-) are placed at k/δ on the abscissa, highlighting the location of the roughness crest.

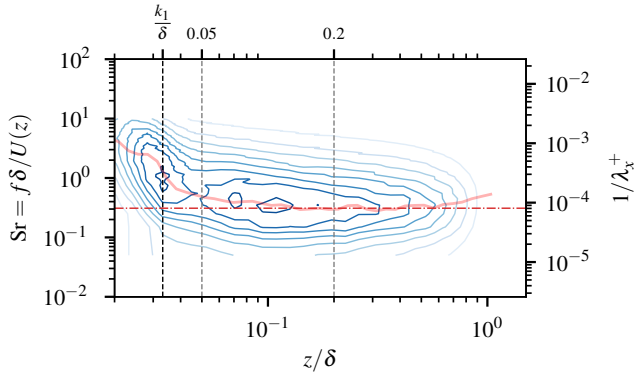

Figure 9: Pre-multiplied spectral map $fS_{uu}(z,f)/U_\tau^2$ obtained by HWA on the rough configuration R1 at $\delta^+ \approx 3800$. The ridge of maximum intensity is displayed using a thick red line (——). The dashdot red line (-·-·-) indicates the Strouhal number $\mathrm{Sr} = 0.3$. The vertical dashed gray lines (- - -) indicate $z/k = 1$, $z/\delta = 0.05$ and $z/\delta = 0.2$ respectively.

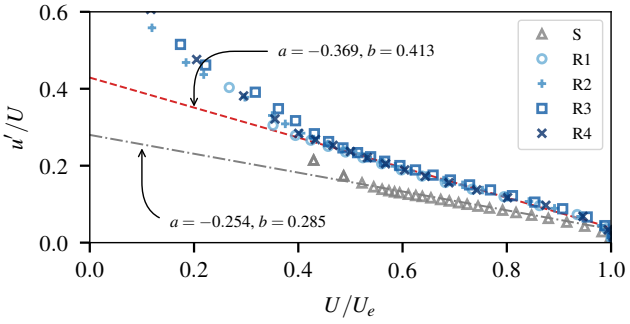

Figure 10: Diagnostic plots obtained from PIV measurements on the smooth case (S) and the four rough configurations (R1 to R4). The dashdot grey line (-·-·-) and the dashed red line (- - -) indicate the linear regressions proposed in the literature for smooth-wall and fully-rough TBL [49, 13].

of $\kappa = 0.39$ and $A = 4.3$ selected in the present work to describe the log-law of a TBL over a smooth wall should be used for consistency instead of κ^* and A^*, while keeping $B = 8.48$. Following this convention yields $k_s^+ \approx 280$ and $k_s/k \approx 2.2$ as reported in Table 1.

This value of $k_s^+ > 70$ indicates that a fully-rough regime is reached. Furthermore, the diagnostic plot shown in Fig. 6 shows a satisfactory agreement between the velocity measurements and the linear regression proposed by Castro et al. [13] for well-behaved fully-rough TBLs. We note however that this configuration yields $\delta/k_s \approx 14$ and $\delta/z_0 \approx 370$, ratios that are respectively lower and larger than the approximate thresholds given in Sect. 1 and proposed by Schultz and Flack [12] and Castro et al. [13] as criteria to ensure wall-similarity. The present rough configuration thus appears as a case for which wall-similarity cannot be guaranteed based on such results. Further analysis regarding this point is provided in Sect. 3.3 where the effect of increasing roughness height is explored.

The value of $k_s/k \approx 2.2$ here obtained lies in-between the estimates provided by Dirling [3] or van Rij et al. [5] ($k_s/k \approx 1.7$) and Waigh and Kind [4] ($k_s/k \approx 2.4$). The corresponding relative differences are respectively of about 20% and 10%. Combining Eq. (4), Eq. (14) and the velocity-defect law for fully-rough zero-pressure-gradient TBL, one can write

$$\sqrt{\frac{2}{C_f}} = \frac{1}{\kappa}\log\left(\frac{\delta}{k}\frac{k}{k_s}\right) + C \tag{15}$$

with $C = 2\Pi/\kappa + B$. Using this relation, these relative differences on k_s/k yield maximum relative differences on C_f of about 4%, a maximum error that was found to hold for the other rough configurations explored. These empirical estimates of k_s/k may then be considered as relatively and equally satisfactory for the present roughness configurations given the large spectrum of roughness element geometry considered to derive these correlations.

The effect of the roughness elements on r.m.s. axial velocity profiles can be observed by comparing Fig. 5b and Fig. 8b. While r.m.s. amplitudes in the outer region of the TBL were not significantly modified (for $z > 0.05\delta$), the presence of the roughness elements significantly altered the inner one, replacing the inner-peak induced by near-wall streaks by a roughness-induced inner-peak of lesser amplitude located at the roughness crest altitude. These modifications are particularly emphasized by examining the pre-multiplied spectral map shown in Fig. 9 in comparison with Fig. 7 obtained for the smooth-wall case. One can observe that the roughness elements induced a clear inner-peak on this spectral map at the roughness crest altitude $z = k$ and at a Strouhal number $\mathrm{Sr} \approx 1$. Compared to the smooth-wall case, a more prominent second outer-peak appears at $z/\delta \approx 0.1$ and $\mathrm{Sr} \approx 0.3$, yielding a spectral ridge in the logarithmic and outer regions closely coinciding with this value of Strouhal number already reported for the smooth-wall case in Sect. 3.1. This suggests that this rough configuration R1 promoted energetic structures characterized by spatial and temporal scales well separated from the ones associated with TBL large-scale structures. Compared to the smooth-case, it may then be speculated that the apparent emergence of the second peak in Fig. 9 is not associated with an intensification of the LSS induced by an interaction with roughness elements (the overall r.m.s. amplitudes are similar in the outer region of the TBLs), but rather the consequence of a decrease of the inner-peak intensity together with a slight increase of the friction Reynolds number δ^+ that promotes the activity of LSS as shown by Hutchins and Marusic [51] on smooth-wall TBLs.

3.3. *Increasing values of k/δ*

Having discussed the overall aerodynamic effects induced by distributed hemispherical roughness elements in Sect. 3.2, we now highlight the consequences of increasing the ratio of roughness height k to TBL thickness δ.

As shown in Table 1, the present experiment covered ratios of δ/k ranging from 30 to 10, and thus ratios of k/δ ranging from 3% to 10%. The four rough configurations yielded approximately equivalent values of friction Reynolds number $\delta^+ \approx 4000$ and values of roughness function ΔU^+ ranging between 10 and 13. This corresponds to values of k_s^+ ranging

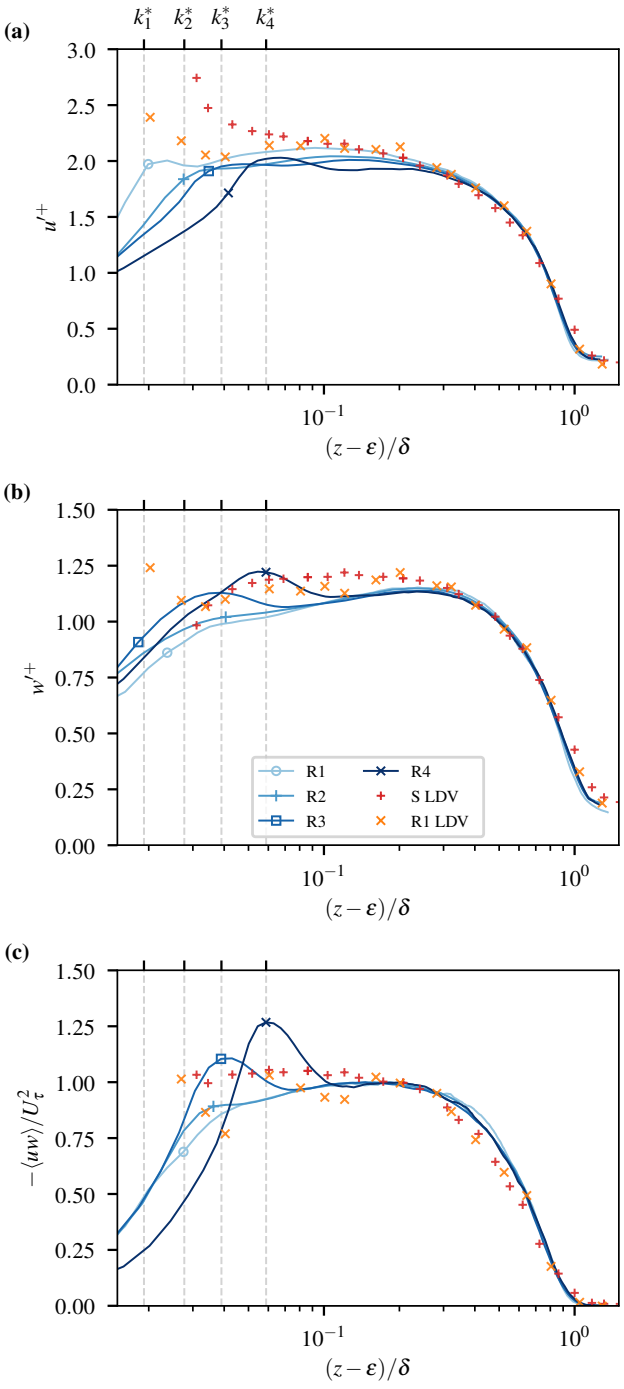

Figure 11: Effect of varying k/δ at approximately matched δ^+ on profiles of **(a)** r.m.s. amplitude of axial velocity, **(b)** r.m.s. amplitude of vertical velocity and **(c)** Reynolds stress measured by stereo-PIV (darker blue solid lines as k/δ increases). For comparison, LDV measurements obtained on cases S (+) and R1 (×) are also displayed. The profiles are plotted as a function of $(z-\varepsilon)/\delta$ to account for the estimated rough-wall correction of origin ε. Vertical gray dashed lines indicate the locations of the roughness crests with $k_i^* \equiv (k_i-\varepsilon)/\delta$.

from 300 to 900 approximately. Interestingly, these four configurations provided almost similar values of k_s/k and z_0/k, suggesting that ratios of k/δ as high as 10% with the present arrangement of roughness elements did not significantly alter the aerodynamic mechanisms at work. To some extent, these four cases are thus all likely representative of fully-rough TBLs, as further discussed in the following paragraph. It may then be concluded that, for the present roughness geometry, the previously discussed correlations that provide estimates for k_s/k are still approximately valid for such large values of k/δ.

The fully-rough state of the TBLs is further evidenced using the diagnostic plots shown in Fig. 10 where the four rough configurations yield overlapping plots that compare very favorably with the linear regression proposed by Castro et al. [13] for fully-rough TBLs in the range $0.5 < U/U_e < 1$. We note nonetheless that the values of TBL wake parameter Π given in Table 1 are overall closer to 0.6 than 0.5 as classically found in smooth-wall TBLs. Such higher values of Π for rough-wall TBLs were previously reported by Krogstad et al. [44] or Castro et al. [13] for instance, the latter authors suggesting that this result may be an indication of a partial lack of similarity between such smooth and rough cases. As discussed in Sect. 1, Castro et al. [13] proposed to consider $\delta/z_0 > 300$ as a criterion to ensure sufficient scale separation and thus proper wall-similarity. For reference, the present rough cases covered values of δ/z_0 ranging from 150 to 370, thus with values below this approximate limit. Equivalently, values of δ/k_s ranged from 5 to 14, thus significantly below the threshold $\delta/k_s \geq 25$ proposed by Schultz and Flack [12] to ensure wall-similarity.

To further investigate the relevance of wall-similarity on these rough configurations, spanwise-averaged r.m.s. amplitude velocity profiles and Reynolds stress profiles obtained by PIV are compared in Fig. 11. Mean axial velocity profiles are not presented for conciseness as they are less discriminant. These profiles, made dimensionless using outer variables, clearly show an excellent collapse for the four rough cases in the outer region of the TBLs, for $z/\delta > 0.2$. The effect of increasing the relative size of the roughness elements is well observed only in the inner region and is characterized by increasing peak amplitudes in w'^+ and $-\langle uw\rangle^+$ at altitudes k/δ. In contrast, the profiles of u'^+ do not depict such a trend. Despite the strong perturbations induced by the largest value of k/δ, the outer region of the TBL does not appear to be significantly influenced, supporting a concept of similarity between these different rough cases. However, compared to the smooth-wall case, slight discrepancies may be observed in the TBL outer region, particularly in the profiles of u'^+ and $-\langle uw\rangle^+$ for $z/\delta > 0.3$. Note here that the smooth-wall LDV measurements for fluctuation quantities are displayed rather than the PIV ones, the latter being over-filtered as previously highlighted in Fig. 5(c). The observed differences are minute for the profiles of u' and may be induced by measurement uncertainties or by differences of friction Reynolds numbers between the smooth ($\delta^+ = 2100$) and the rough cases ($\delta^+ \approx 4000$). This observation appears nonetheless consistent with the previous remark made on the values of the wake parameter Π, suggesting again that wall-similarity may not be perfectly achieved even

if a very satisfactory similarity between the rough cases is observed. The discrepancy between smooth and rough-wall TBLs outer regions appears more pronounced at first sight for the profiles of $-\langle uw\rangle^+$ but it is likely induced by the uncertainties or measurement errors associated with PIV and LDV techniques in measuring this stress. Indeed, one can observe that the LDV measurements obtained for cases S and R1 collapse satisfactorily in the outer region, suggesting close similarity between the two configurations, while the case R1 is observed to compare very favorably with the other rough cases investigated by PIV. Overall, despite these slight discrepancies, we argue that wall-similarity still provides a reasonable assumption for such rough configurations and that the main aerodynamic mechanisms driving turbulence in the TBLs outer region were not substantially altered.

These observations lend support to the idea that the various step changes in roughness condition induced by the surface geometries detailed in Sect. 2.2 and generating internal boundary layers (IBLs) are performed sufficiently upstream of the measurement location to provide fully-developed TBLs over the third rough plate. If Δx_i refers to the axial distance between the present velocity measurement location and the location of the final step change in configuration Ri, the minimum value of the ratio $\Delta x_i/z_0$ is obtained for the case R4 (see Table 1 for values of z_0) and amounts to 1300. For comparison, Cheng and Castro [53] reported near-self-preserving TBL states sustaining large step changes in roughness condition for $\Delta x/z_0 \approx 300$ for their particular case of study. Without generalizing this result, it nonetheless suggests that all the TBLs here examined are likely well adapted to the roughness geometry at the measurement location. This point is particularly supported by considering that the cases R2 to R4 compare very satisfactorily with the case R1 where only one step change from a smooth to a rough surface was prescribed and where the streamwise development of the IBL was about 30δ, corresponding to $10^4 z_0$. We further note that no significant effect associated with upstream IBLs should be expected since IBLs develop a priori independently of upstream TBL conditions when a step change is made to a rougher surface [26, 54, 55]. Finally, it is emphasized that the present results were obtained at relatively large values of k_s^+ and δ^+, thus well into the fully-rough regime and with significant inner-outer scale separations. Different behaviors may then be expected for lower values, particularly if transitionally-rough regimes are considered or if ratios δ/k_s are not *large* enough, the definition of which being likely geometry-dependent.

Supporting evidence for the previous statement that wall-similarity approximately applies is provided by examining the pre-multiplied spectral maps deduced from HWA measurements and shown in Fig. 12 for the rough configurations R3 and R4. Compared to Fig. 9 that provided results for the configuration R1, one can observe the displacement of the energetic inner-site induced by the growing roughness elements. The spectral ridge in the outer region of the TBLs appears however to remain very close to a constant value $\mathrm{Sr} \approx 0.3$ as in the smooth-wall case. It can then be postulated that the spectral characteristics of the fluctuations induced by the roughness elements are sufficiently separated from the ones of the TBL LSS

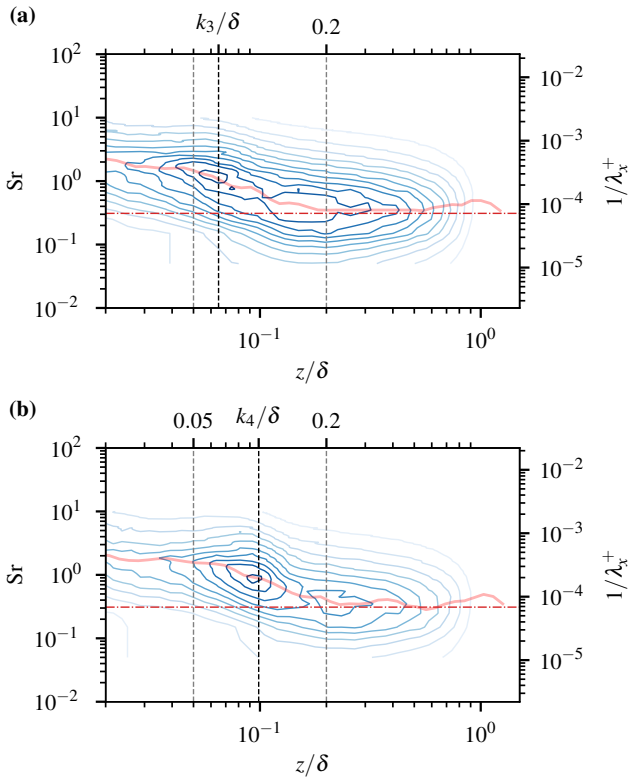

Figure 12: Pre-multiplied spectral maps obtained by HWA on the rough configurations **(a)** R3 and **(b)** R4. Refer to Fig. 9 for the legend.

to prevent a direct coupling, ensuring a (quasi) wall-similarity even for $k/\delta = 10$ with the present roughness geometry.

This conclusion is finally supported by examining the vertical and spanwise two-point correlation coefficient profiles of axial and vertical velocity, respectively noted R_{uu} and R_{ww}, shown in Fig. 13. These correlation coefficients are evaluated relying on the PIV measurements by considering a reference point at a vertical location well into the TBL outer region at $z_{\mathrm{ref}} = 0.5\delta$. A satisfactory collapse of all the profiles is obtained, suggesting no major changes between smooth and rough cases in the vertical and spanwise structure of the energy-containing eddies evolving in the TBL outer region. Comparisons with spanwise correlation profiles reported by Hutchins and Marusic [51] and Ganapathisubramani et al. [56] at a similar reference altitude (but different values of δ^+) and for smooth-wall TBLs are shown in Fig. 13(b) and Fig. 13(d), providing confidence in the estimated correlations.

4. Temperature profiles and heat transfer results

4.1. Analysis of the temperature profiles

Mean flow temperature profiles were acquired for each rough configuration at an axial location similar to the one used in the previous aerodynamic analysis. For each acquisition point, the external flow temperature T_e was also recorded. The average wall temperature T_w was estimated relying on IR thermography (as described in Sect. 2.5) by spatially averaging the measured

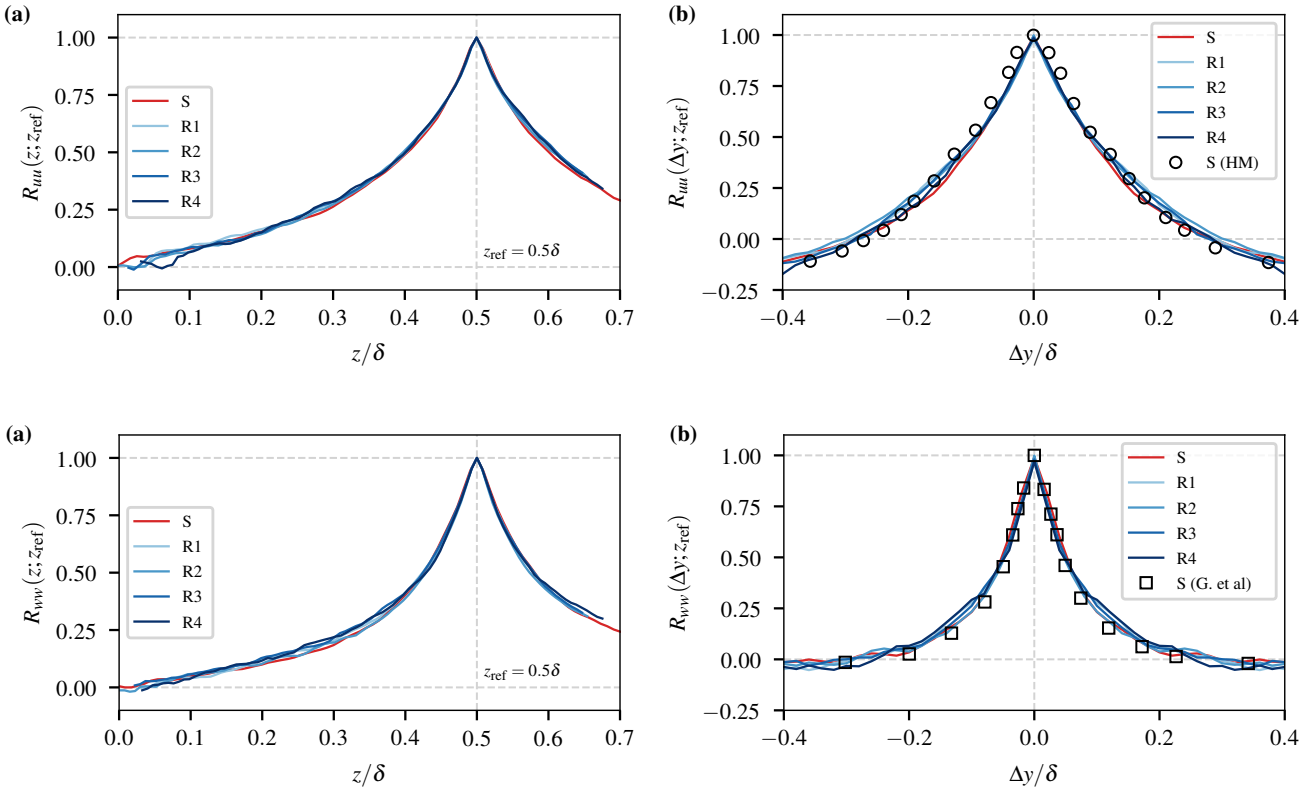

Figure 13: **(a,c)** Vertical and **(b,d)** spanwise profiles of two-point correlation coefficients of axial and vertical velocity (R_{uu} and R_{ww} respectively) evaluated with a reference point at an altitude $z_{\mathrm{ref}}/\delta = 0.5$ relying on the PIV data for the smooth and the rough cases. In **(b)** is also displayed a R_{uu} profile measured by Hutchins and Marusic [51] in a smooth-wall TBL at $\delta^+ = 7600$ while in **(d)** is displayed a R_{ww} profile measured by Ganapathisubramani et al. [56] in a smooth-wall TBL at $\delta^+ = 1100$.

mean surface temperature distribution over several patches of roughness elements. As observed in Fig. 14, the surface temperature distribution is not uniform for stationary flow conditions because of the moderate thermal conductivity of the material used to manufacture the rough plates. The estimated average wall temperature thus accounts for such temperature differences existing between the 3D roughness elements and the flat plate. As explained in Sect. 2.6, such a 3D distribution is however difficult to accurately capture using the present IR thermography setup. As a consequence, the estimated value of T_w can only be accurate within a few degrees, with a maximum estimated uncertainty of about $\pm 2\,^{\circ}\mathrm{C}$.

The profiles of mean flow temperature difference $(T_w - T)$ measured on the four rough configurations using cold-wire thermometry are displayed in Fig. 15 using two layouts that help comparing them with results found in the literature. Fig. 15(a) shows the mean temperature profiles made dimensionless using the temperature difference across the boundary layer $(T_w - T_e)$ and the enthalpy thickness Δ_2 defined as

$$\Delta_2 \equiv \int_0^\infty \frac{U(z)}{U_e}\left(\frac{T(z)-T_e}{T_w-T_e}\right)\mathrm{d}z\,. \tag{16}$$

The velocity profiles used to evaluate Δ_2 are the ones measured by PIV and reported in Sect. 3. A clear overlap of the measurements obtained on the four rough surfaces is observed, indicating similarity between these profiles. A logarithmic region is observed over a significant spatial extent, with a slope estimated using a logarithmic regression over that region that compares favorably with the data reported by Pimenta et al. [57] and Ligrani and Moffat [16]. Some discrepancies nonetheless exist, these two reference studies having focused on different configurations. Pimenta et al. [57] studied a rough surface made of closely-packed spheres and such that the entire length of the rough flat plate was heated, providing almost matched dynamic

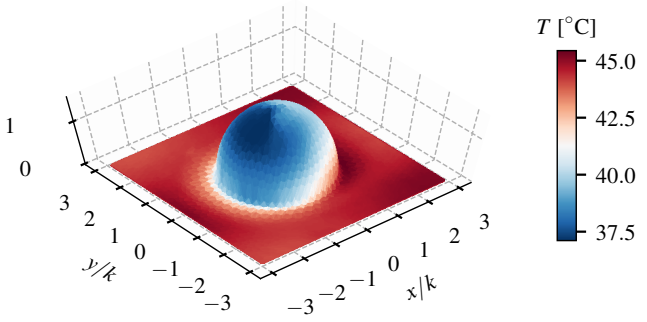

Figure 14: Mean temperature distribution over a roughness element measured by IR thermography on configuration R4 at the end of a transient aerodynamic and thermal response using the setup described in Sect. 2.5.

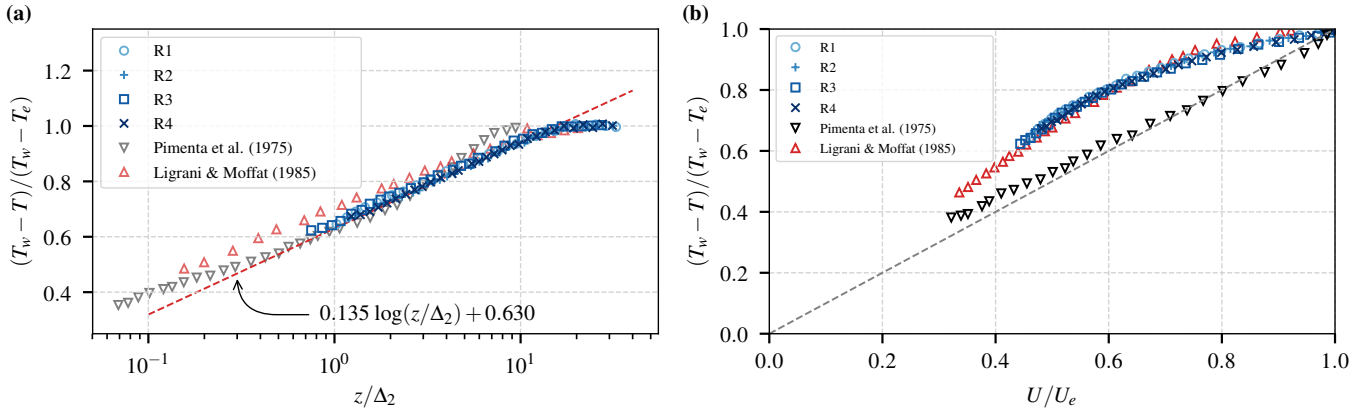

Figure 15: Profiles of mean temperature difference measured by cold-wire thermometry on the four rough configurations listed in Table 1. **(a)** Temperature profiles made dimensionless using the temperature difference across the TBL $(T_w - T_e)$ and the enthalpy thickness Δ_2, compared with the experimental results reported by Pimenta et al. [57] and Ligrani and Moffat [16] without and with unheated starting-length respectively. The dash red line (- - -) indicates a logarithmic fit of the present data over $z/\Delta_2 \in [1, 10]$. **(b)** Mean temperature profiles as a function of mean velocity measured by PIV and compared with the same references used in Fig.(a); the dashed gray line provides the identity map.

and thermal boundary layer thicknesses. Ligrani and Moffat [16] used the same roughness configuration as Pimenta et al. [57] but investigated the effect of having an unheated starting length ξ as in the present work. A consequence of the unheated starting length $\xi > 0$ is that the thermal boundary layer is contained inside the dynamic TBL and does not display a wake region: the logarithmic law directly fades into a constant temperature profile at $z \approx \Delta_2$ as in the work of Ligrani and Moffat [16], while the profiles reported by Pimenta et al. [57] clearly display a wake region. The similarity of the present results with the ones reported by Ligrani and Moffat [16] is more evident on the $T-U$ plot given in Fig. 15(b). This figure represents the same mean temperature measurements but as a function of local mean axial velocity measured by PIV, the latter being interpolated at locations of the former. Here again, an excellent collapse of the present data is obtained and a favorable agreement is observed with the profiles reported by Ligrani and Moffat [16]. The departure from the almost linear trend observed by Pimenta et al. [57] and represented in Fig. 15(b) using a dashed line is the consequence of the unheated starting length yielding a lack of local similarity between dynamic and thermal boundary layers. Two main conclusions may then be drawn from these results. First, the present setup that induced a step-change in surface temperature and several step changes in roughness conditions provided TBLs and thermal boundary layers that have some characteristics well in line with results found in the literature where only one step change in both temperature and roughness conditions were imposed [16]. It may then be suggested that the present work provides results that are not significantly dependent on the way such roughness and temperature step changes were applied. At the measurement location studied, some degree of universality regarding aerodynamic and thermal effects induced by roughness elements can thus be expected as in the work of Ligrani and Moffat [16]. This conclusion is used in the following discussion to support the relevance of the present measurements to analyze trends in inner-normalized temperature profiles. Second, the estimated values of mean surface temperature T_w obtained by IR thermography allowed to satisfactorily collapse the temperature profiles in a way that is consistent with the literature, suggesting that no significant bias was introduced with this approach despite the complex temperature distribution existing over the roughness elements.

The measured mean temperature profiles are now analyzed to investigate the effect of increasing the relative height of roughness elements on characteristics of the thermal boundary layer. The friction temperature T_τ was estimated for each rough configuration by fitting Eq. (10) to the data, assuming $\kappa_\theta = 0.48$ and defining the thermal boundary layer thickness δ_T such that $T(\delta_T) = 0.99T_e$. Note that using Eq. (10) instead of the temperature law of the wall expressed in the following Eq. (17) ensures that estimated values of T_τ do not depend on T_w but rather on T_e whose value is less uncertain. The resulting profiles are shown in Fig. 16(a), highlighting a good collapse of the four rough cases and a correct logarithmic trend over the entire thermal boundary layer thickness. Relying on these estimated values of T_τ, inner-normalized temperature profiles $\theta^+ \equiv (T_w - T)/T_\tau$ are shown in Fig. 16(b) as a function of z/k_s. It was shown by Kays and Crawford [21] and Ligrani et al. [20] that the logarithmic region of such profiles is well represented by the fully-rough temperature law of the wall expressed as

$$\theta^+ = \delta\theta^+ + \mathrm{Pr}_t \left(\frac{1}{\kappa} \log \frac{z}{k_s} + B \right). \tag{17}$$

This expression may also be written in the following form,

$$\theta^+ = \frac{1}{\kappa_\theta} \log z^+ + A_\theta - \Delta\theta^+ \tag{18}$$

where

$$\Delta\theta^+ = \mathrm{Pr}_t \Delta U^+ - \delta\theta^+ \tag{19a}$$

$$= \frac{1}{\kappa_\theta} \log k_s^+ + A_\theta - B_\theta - \delta\theta^+ \tag{19b}$$

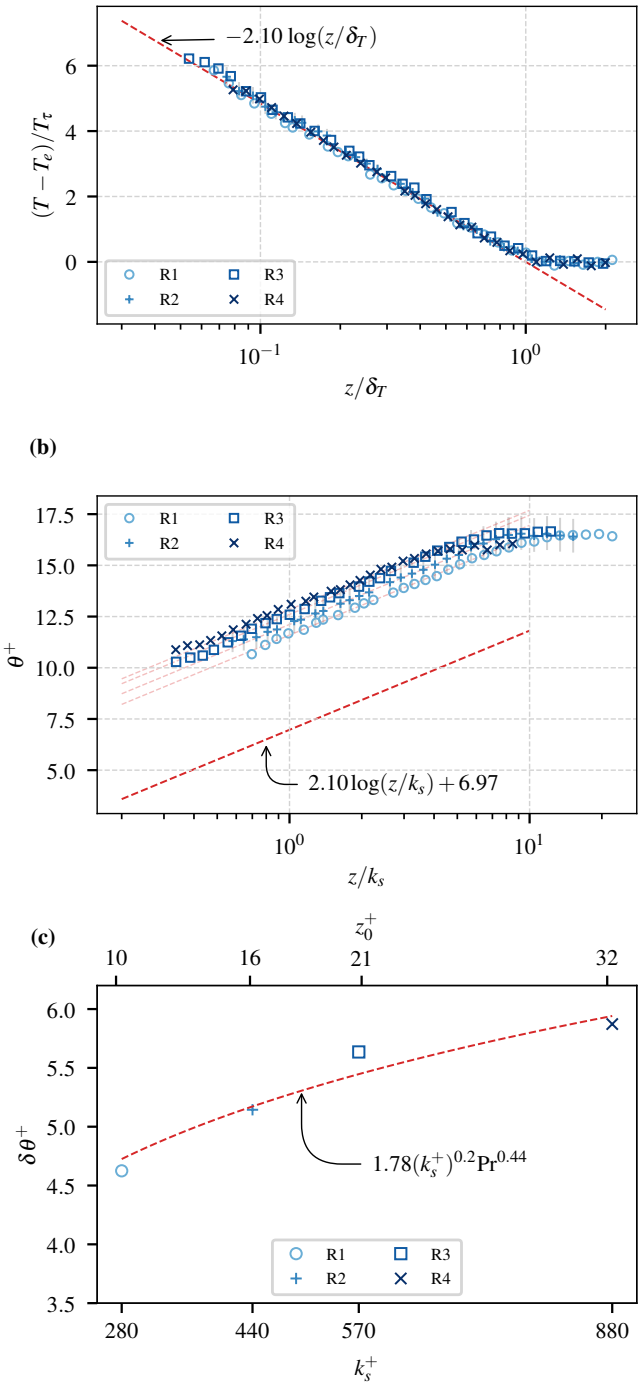

Figure 16: **(a)** Temperature profiles measured by cold-wire thermometry and made dimensionless using the friction temperature T_τ for the four rough configurations listed in Table 1; the red dashed line represents a logarithmic fit on the data. **(b)** Inner-normalized mean temperature profiles as a function of z/k_s for the four rough cases; the red dashed line provides the smooth-wall temperature law of the wall. **(c)** Non-dimensional wall temperature step $\delta\theta^+$ deduced from (b) for the four rough configurations; the law given by Eq. (20) with $C = 1.78$ is plotted using a red dashed line.

is the rough-wall temperature shift compared to the smooth case, with $A_\theta \approx 3.5$ and $B_\theta = \mathrm{Pr}_t B \approx 7$ with $\mathrm{Pr}_t = 0.82$ (Sect. 2.6). In these relations, $\delta\theta^+$ is termed the non-dimensional wall temperature step [16] and is expected to depend on the roughness geometry. This wall temperature step accounts for the fact heat transfer at the wall can only be achieved by molecular conduction, even in the fully-rough regime, highlighting the difference of mechanism compared to momentum transfer at the wall. In this regime, an important consequence is that $\Delta\theta^+$ does not display a log-linear asymptotic trend like ΔU^+ and that one needs to identify $\delta\theta^+$ to correctly model heat transfer. As reported by Kays and Crawford [21], one may rely on the work of Dipprey and Sabersky [19] to provide a semi-empirical expression for $\delta\theta^+$ that reads

$$\delta\theta^+ = C\,(k_s^+)^{0.2}\,\mathrm{Pr}^{0.44} \tag{20}$$

where C is a parameter that depends on the properties of the surface roughness and Pr is the Prandtl number of the fluid. Notably, Ligrani and Moffat [16] showed that $C \approx 1$ provided satisfactory results for rough surfaces made of packed spheres. In the present case of distributed hemispheres, much less is known about the relevance of Eq. (20).

Interestingly, Ligrani and Moffat [16] also concluded that the magnitude of unheated starting length did not influence the logarithmic region of the thermal boundary layer, preserving the fully-rough temperature law of the wall given by Eq. (17). It can thus be expected that the present profiles displayed in Fig. 16(b) are adequate to investigate the thermal effect induced by hemispherical roughness elements. In this figure, compared to the smooth-wall case where $\delta\theta^+ = 0$ highlighted using a red dashed line, increasing the relative roughness size and thus k_s^+ (see Table 1) yields a progressive increase of the temperature shift in the logarithmic region. The associated values of $\delta\theta^+$ are displayed in Fig. 16(c) as a function of k_s^+. Using Eq. (20), a satisfactory fit was obtained for $C = 1.78$ assuming $\mathrm{Pr} = 0.71$ for air. Note that given the uncertainties on the values of Pr_t and κ used to evaluate $\delta\theta^+$, we estimate the uncertainty on C to be around ± 0.1.

The conclusion of this section is twofold. First, it appears that a relationship as given by Eq. (20) is adequate to describe the temperature shift induced by distributed hemispherical roughness elements over the range of k_s^+ values investigated. Second, while Ligrani and Moffat [16] found a parameter $C \approx 1$ in Eq. (20) for rough surfaces made of packed spheres, the present study suggests that a higher value $C \approx 1.78 \pm 0.1$ should be considered for the present configuration of distributed hemispherical roughness elements.

4.2. Heat transfer coefficients and Stanton numbers

Heat transfer coefficients h were estimated for each rough configuration relying on the two methods detailed in Sect. 2.6. The resulting Stanton numbers St are displayed in Fig. 17 using three different layouts. Fig. 17(a) provides a comparison of the estimated values of St obtained as a function of the ratio of roughness height k to thermal boundary layer thickness δ_T. Error bars with amplitudes of $\pm 3.5\%$ are also displayed, corresponding to the uncertainty with 95% CI estimated in Sect. 2.6

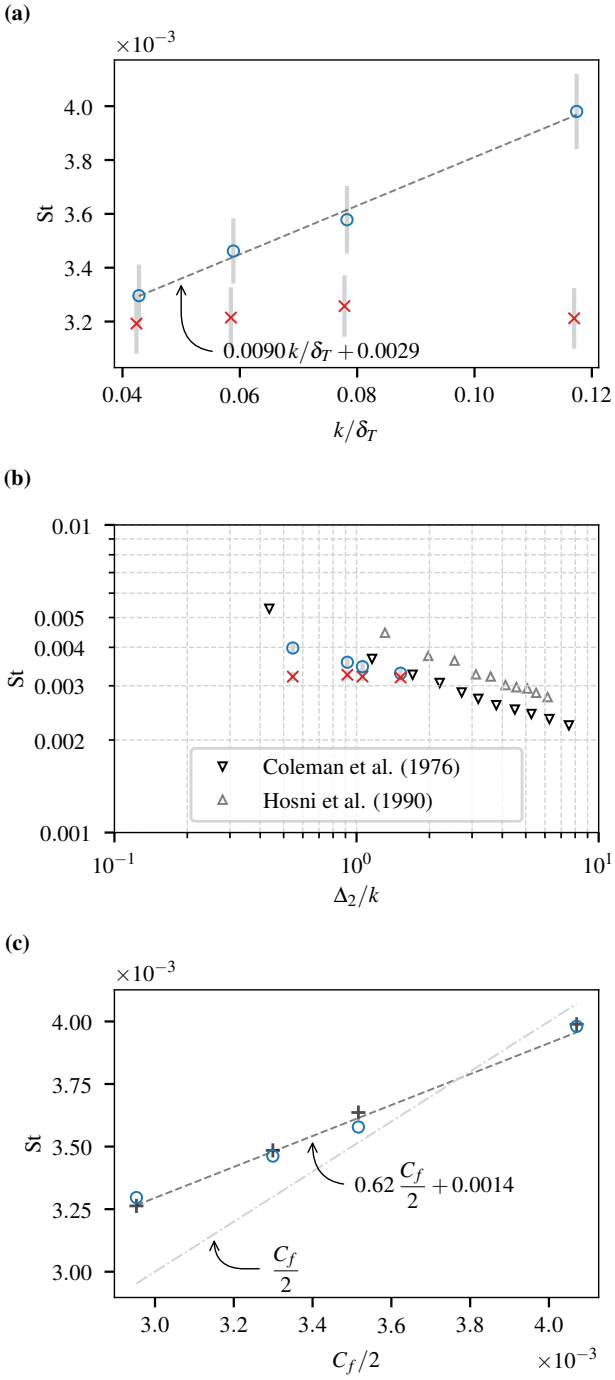

Figure 17: Estimated values of Stanton number St on the four rough configurations listed in Table 1 using the two methods described in Sect. 2.6: (○): method based on mean temperature profiles; (×): method based on heat transients. **(a)** Effect of varying k/δ_T; the dashed line correspond to a linear regression on the values yielded by the first method; error bars have a relative amplitude of $\pm 3.5\%$. The data obtained with the second method were slightly transferred leftward to avoid overlapping of error bars. **(b)** Comparison of the present estimates with St values reported by Coleman et al. [58] and Hosni et al. [17]. **(c)** Estimated values of St as a function of the friction coefficient $C_f/2$; a linear regression on the data is displayed using a dashed gray line (- - -) while values obtained using Eq. (21) are given by dark crosses (+).

for the method relying on temperature profiles. Clearly, the two estimation approaches provide different trends. On one hand, the method relying on the mean temperature profiles (hereby referred to as the first approach) suggests a linear trend with a positive slope, the best linear fit being indicated in the figure. On the other hand, the method relying on heat transients and surface temperature measurements performed by IR thermography (referred to as the second approach) yields an almost constant value $\mathrm{St} \approx 0.0031$ over the range of k/δ_T explored. Based on the discussion conducted in Sect. 2.6 regarding uncertainties associated with each approach, we believe that the most questionable results should come from the second approach where 3D diffusion effects were neglected. To support this claim, a comparison of the present results with Stanton numbers reported by Coleman et al. [58] on packed-spheres roughness and Hosni et al. [17] on hemispherical roughness elements is shown in Fig. 17(b). This figure is plotted in log-log coordinates and shows St as a function of Δ_2/k. A monotonic decreasing trend is observed on the data reported in the literature which appears to be consistent with the results yielded in our work by the first estimation approach. Such a trend was also reported by Ligrani and Moffat [16] on packed-spheres with unheated starting length, suggesting again that the plateau of St obtained in the present work with the second approach is likely doubtful. The following discussion will thus assume that the correct values of St are the ones obtained using the first approach based on mean temperature profiles. We suggest that the results obtained with the second estimation approach relying on surface temperature transients should be considered with care and that a more detailed analysis of the possible uncertainties associated with this approach is necessary, at least for configurations similar to the ones here studied.

Further analyzing Fig. 17(b), it can be observed that our estimated values of Stanton number follow a linear trend located below the one reported by Hosni et al. [17] who studied a roughness configuration very similar to the present one. As discussed by Ligrani and Moffat [16], this is the consequence of the unheated starting length $\xi > 0$ in the present experiment, Hosni et al. [17] having considered an isothermal configuration. This dependence of St on ξ prevents us from providing further conclusions on the associated trends as only one value of ξ was investigated. It is nonetheless instructive to examine Fig. 17(c) where St as a function of $C_f/2$ is displayed. The measurements provide an almost linear relationship such that $\mathrm{St} \approx 0.62\left(C_f/2\right) + 0.0014$ over the range of friction coefficient explored. This relationship is expected to change as ξ is modified following the results shown in Fig. 17(b). Combining Eq. (12), Eq. (13) and Eq. (17), the Stanton number can also be expressed as a function of the friction coefficient as

$$\mathrm{St} = \frac{\sqrt{C_f/2}}{\delta\theta^+ + \mathrm{Pr}_t\left(\frac{1}{\kappa}\log\frac{\delta_T}{k_s} + B\right)}, \tag{21}$$

where the effect of the unheated starting length is taken into account by the ratio δ_T/k_s. The points obtained using this relation with a constant parameter $C = 1.78$ in Eq. (20) are also displayed in Fig. 17(c), showing an excellent agreement with

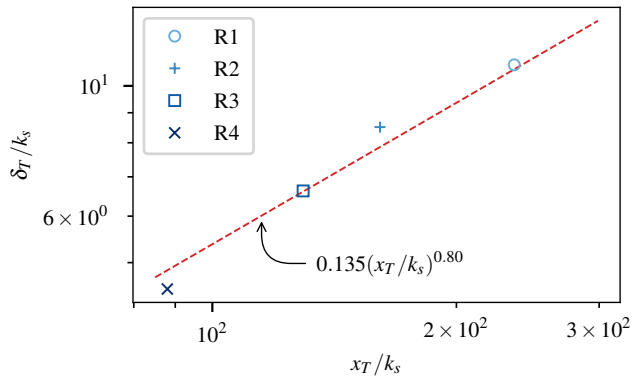

Figure 18: Ratio of thermal boundary layer thickness to equivalent sand grain height δ_T/k_s as a function of x_T/k_s for the four rough cases, where $x_T \approx 660$mm refers to the streamwise extent of the thermal boundary layer (from the start of the second rough plate to the measurement location). The red dashed line displays a power law of the type $\delta_T/k_s = a(x_T/k_s)^n$ with $a = 0.135$ and $n = 0.8$.

the measurements. Such an agreement was expected since the same temperature profile measurements were used to obtain values for C and St. Still, it highlights the consistency of the results obtained on the four rough configurations and the validity of using a constant value for C in the semi-empirical relation for $\delta\theta^+$. It finally emphasizes the well known fact that the Reynolds analogy classically assumed for smooth-wall configurations and yielding the relation $\mathrm{St} = C_f/2$ cannot be applied for such rough cases.

Using Eq. (21) for a modeling purpose requires to estimate C_f, $\delta\theta^+$ and δ_T/k_s. The first two parameters can be easily obtained using the previous aerodynamic and thermal results (see equations (15) and (20) for instance), leaving the ratio δ_T/k_s to discuss. This quantity is plotted in Fig. 18 as a function of x_T/k_s for the four rough cases, with x_T the streamwise extent of the thermal boundary layer to the measurement location. A power law with an exponent $n = 0.8$ provides a satisfactory fit to the data. Such an exponent is in agreement with previous works performed on the subject of step change in surface heat flux [59, 60] where a similar exponent was reported. Further investigation on this result is required since, contrary to cases R1 and R2, the thermal IBLs for cases R3 and R4 sustained a step change in surface roughness that could have significantly altered their growth. We suggest nonetheless that such an empirical result can provide an approximate way of estimating δ_T/k_s and thus St for roughness geometries and temperature changes similar to the ones investigated in this work.

5. Conclusion

Aerodynamic and thermal effects induced by relatively large hemispherical roughness elements inducing step changes in surface roughness and temperature conditions on a TBL were experimentally analyzed in two distinct parts.

The aerodynamic part showed first that stereo-PIV and HWA were adequate in measuring velocity fluctuations induced by such rough surfaces down to the roughness elements crests, the characteristic length scale of the induced energy-containing eddies being of the same order of magnitude as the laser sheet width and the hot-wire length. Second, an excellent outer-layer similarity was observed on mean and r.m.s. velocity profiles between the four rough cases investigated. Yet, slight discrepancies were reported compared to a smooth-wall case, suggesting that wall-similarity was not perfectly achieved. These differences are nonetheless minute and spectral maps of axial velocity and two-point correlation profiles suggested that roughness elements did not significantly interact with the LSS developing in the outer-layer of the TBLs. Interestingly, the rough case with the smallest roughness height provided spectral maps with an outer peak more readily observable than in a smooth-case as the inner-peak induced by roughness elements was less intense than the one generated by near-wall streaks. Third, as a consequence of the observed quasi-wall-similarity, the present configurations were all considered as fully-rough TBLs despite the small ratios $\delta/k < 30$ and $\delta/k_s < 15$ obtained. It was finally shown that empirical correlations proposed in the literature [3, 4, 5] to estimate values of k_s/k provide reasonable results for the present configurations if one tolerates an error on C_f of about 4%.

The second part of this work showed that temperature profiles obtained on such partially-heated rough configurations could be used to analyze the corresponding fully-rough temperature law of the wall. The relation proposed in the literature [19, 16, 21] for the wall temperature step $\delta\theta^+$ was reported to satisfactorily describe the data and a value of 1.78 ± 0.1 for the roughness-dependent parameter C appearing in this semi-empirical relation was estimated for the present roughness geometry. This value is significantly different from the one reported in the literature for packed spheres, that was $C \approx 1$ [20]. Furthermore, two heat transfer estimation methods were compared. It was suggested that care should be taken when using rough surface temperature transients and a simplified surface geometry for the conduction problem to solve. We suggest that a more detailed numerical analysis of this approach should be considered for future investigations. The second method based on mean temperature profile measurements yielded satisfactory results with trends that compared favorably with the literature when one accounts for the effect of an unheated starting length [17, 16]. Building on these results, a semi-empirical relation for $\mathrm{St}(C_f)$ accounting for $\delta\theta^+$ and the presence of a thermal internal boundary layer developing after an unheated starting length was derived and compared satisfactorily with the measurements. Considering the two parts of this study, the present work thus suggests that despite the relative large size of the roughness elements considered, the aerodynamic and the thermal behavior (in terms of C_f and St) of TBLs developing over such rough surfaces can be satisfactorily modeled relying on known or modified semi-empirical relations, which can prove useful in a modeling perspective.

Acknowledgments

This work was performed in the framework of the Physice 2 project financed by the Direction Générale de l'Aviation Civile (DGAC), France, and in the framework of the ROOTT project at ONERA/DMPE. The authors warmly thank C. Fort for his initial work on the aerodynamic part of this article during his internship, F. Micheli for the LDV measurements performed in a previous campaign, D. Donjat for his work on the design of the rough surfaces, D. Toussaint for fruitful discussions and N. Fasano for his essential technical work on the wind tunnel test-section.

References

[1] H. Schlichting, Experimentelle Untersuchungen zum Rauhigkeitsproblem, Ingenieur-Archiv 7 (1) (1936) 1–34, ISSN 1432-0681, DOI 10.1007/BF02084166.

[2] J. Nikuradse, Strömungsgesetze in rauhen Rohren, VDI-Verlag, also: Laws of flow in rough pipes, NACA-TM-1292, 1950, 1933.

[3] R. Dirling, A method for computing roughwall heat transfer rates on reentry nosetips, DOI 10.2514/6.1973-763, 1973.

[4] D. R. Waigh, R. J. Kind, Improved Aerodynamic Characterization of Regular Three-Dimensional Roughness, AIAA Journal 36 (6) (1998) 1117–1119, DOI 10.2514/2.491.

[5] J. A. van Rij, B. J. Belnap, P. M. Ligrani, Analysis and Experiments on Three-Dimensional, Irregular Surface Roughness, Journal of Fluids Engineering 124 (3) (2002) 671–677, DOI 10.1115/1.1486222.

[6] M. R. Raupach, R. A. Antonia, S. Rajagopalan, Rough-Wall Turbulent Boundary Layers, Applied Mechanics Reviews 44 (1) (1991) 1, DOI 10.1115/1.3119492.

[7] A. Townsend, The Structure of Turbulent Shear Flow, Cambridge Monographs on Mechanics and Applied Mathematics, Cambridge University Press, second edn., 1976.

[8] J. Jimenez, Turbulent flows over rough walls, Annual Review of Fluid Mechanics 36 (1) (2004) 173–196, DOI 10.1146/annurev.fluid.36.050802.122103.

[9] I. P. Castro, Rough-wall boundary layers: mean flow universality, Journal of Fluid Mechanics 585 (2007) 469–485, DOI 10.1017/s0022112007006921.

[10] M. Amir, I. P. Castro, Turbulence in rough-wall boundary layers: universality issues, Experiments in Fluids 51 (2) (2011) 313–326, DOI 10.1007/s00348-011-1049-7.

[11] K. A. Flack, M. P. Schultz, Roughness effects on wall-bounded turbulent flows, Physics of Fluids 26 (10) (2014) 101305, DOI 10.1063/1.4896280.

[12] M. P. Schultz, K. A. Flack, Outer layer similarity in fully rough turbulent boundary layers, Experiments in Fluids 38 (3) (2005) 328–340, DOI 10.1007/s00348-004-0903-2.

[13] I. P. Castro, A. Segalini, P. H. Alfredsson, Outer-layer turbulence intensities in smooth- and rough-wall boundary layers, Journal of Fluid Mechanics 727 (2013) 119–131, DOI 10.1017/jfm.2013.252.

[14] M. Placidi, B. Ganapathisubramani, Turbulent Flow Over Large Roughness Elements: Effect of Frontal and Plan Solidity on Turbulence Statistics and Structure, Boundary-Layer Meteorology 167 (1) (2017) 99–121, DOI 10.1007/s10546-017-0317-3.

[15] M. M. Pimenta, R. J. Moffat, W. M. Kays, The Structure of a Boundary Layer on a Rough Wall with Blowing and Heat Transfer, Journal of Heat Transfer 101 (2) (1979) 193–198, DOI 10.1115/1.3450945.

[16] P. M. Ligrani, R. J. Moffat, Thermal boundary layers on a rough surface downstream of steps in wall temperature, Boundary-Layer Meteorology 31 (2) (1985) 127–147, DOI 10.1007/bf00121174.

[17] M. Hosni, H. W. Coleman, R. P. Taylor, Measurements and calculations of rough-wall heat transfer in the turbulent boundary layer, International Journal of Heat and Mass Transfer 34 (4-5) (1991) 1067–1082, DOI 10.1016/0017-9310(91)90017-9.

[18] M. Hosni, H. W. Coleman, J. W. Garner, R. P. Taylor, Roughness element shape effects on heat transfer and skin friction in rough-wall turbulent boundary layers, International Journal of Heat and Mass Transfer 36 (1) (1993) 147–153, DOI 10.1016/0017-9310(93)80074-5.

[19] D. Dipprey, R. Sabersky, Heat and momentum transfer in smooth and rough tubes at various prandtl numbers, International Journal of Heat and Mass Transfer 6 (5) (1963) 329–353, DOI 10.1016/0017-9310(63)90097-8.

[20] P. Ligrani, W. Kays, R. Moffat, A heat transfer prediction method for turbulent boundary layers developing over rough surfaces with transpiration, International Journal of Heat and Mass Transfer 24 (4) (1981) 774–778, DOI 10.1016/0017-9310(81)90023-5.

[21] W. M. Kays, M. E. Crawford, Convective heat and mass transfert, McGraw-Hill Book, 1993.

[22] R. P. Taylor, H. W. Coleman, B. K. Hodge, Prediction of Turbulent Rough-Wall Skin Friction Using a Discrete Element Approach, Journal of Fluids Engineering 107 (2) (1985) 251–257, DOI 10.1115/1.3242469.

[23] B. Aupoix, Revisiting the Discrete Element Method for Predictions of Flows Over Rough Surfaces, Journal of Fluids Engineering 138 (3), DOI 10.1115/1.4031558.

[24] D. B. De Graaff, J. K. Eaton, Reynolds-number scaling of the flat-plate turbulent boundary layer, Journal of Fluid Mechanics 422 (2000) 319–346, DOI 10.1017/s0022112000001713.

[25] P. M. Ligrani, R. J. Moffat, Structure of transitionally rough and fully rough turbulent boundary layers, Journal of Fluid Mechanics 162 (-1) (1986) 69, DOI 10.1017/s0022112086001933.

[26] R. A. Antonia, R. E. Luxton, The response of a turbulent boundary layer to a step change in surface roughness Part 1. Smooth to rough, Journal of Fluid Mechanics 48 (4) (1971) 721–761, DOI 10.1017/s0022112071001824.

[27] H. Cheng, P. Hayden, A. Robins, I. Castro, Flow over cube arrays of different packing densities, Journal of Wind Engineering and Industrial Aerodynamics 95 (8) (2007) 715–740, DOI 10.1016/j.jweia.2007.01.004.

[28] L. Perret, F. Kerhervé, Identification of very large scale structures in the boundary layer over large roughness elements, Experiments in Fluids 60 (6), DOI 10.1007/s00348-019-2749-7.

[29] H. W. Coleman, B. K. Hodge, R. P. Taylor, A Re-Evaluation of Schlichting's Surface Roughness Experiment, Journal of Fluids Engineering 106 (1) (1984) 60, DOI 10.1115/1.3242406.

[30] K. A. Flack, M. P. Schultz, Review of Hydraulic Roughness Scales in the Fully Rough Regime, Journal of Fluids Engineering 132 (4) (2010) 041203, DOI 10.1115/1.4001492.

[31] P. Reulet, G. Leplat, An inverse method for experimental determination of temperature dependent thermal conductivities and specific heat of orthotropic materials, in: Thermal Conductivity 31/Thermal Expansion 19, DEStech Publications, Inc, 3, 2013.

[32] P. Reulet, B. Aupoix, D. Donjat, F. Micheli, Boundary Layer and Heat Transfer Characterization on a Flat Plate with Realistic Ice Roughness, in: SAE Technical Paper Series, SAE International, DOI 10.4271/2015-01-2096, 2015.

[33] F. Champagnat, A. Plyer, G. L. Besnerais, B. Leclaire, S. Davoust, Y. L. Sant, Fast and accurate PIV computation using highly parallel iterative correlation maximization, Experiments in Fluids 50 (4) (2011) 1169–1182, DOI 10.1007/s00348-011-1054-x.

[34] N. Hutchins, T. B. Nickels, I. Marusic, M. S. Chong, Hot-wire spatial resolution issues in wall-bounded turbulence, Journal of Fluid Mechanics 635 (2009) 103–136, DOI 10.1017/s0022112009007721.

[35] A. Sciacchitano, B. Wieneke, PIV uncertainty propagation, Measurement Science and Technology 27 (8) (2016) 084006, DOI 10.1088/0957-0233/27/8/084006.

[36] B. Efron, R. J. Tibshirani, An introduction to the bootstrap, CRC press, 1994.

[37] I. Marusic, J. P. Monty, M. Hultmark, A. J. Smits, On the logarithmic region in wall turbulence, Journal of Fluid Mechanics 716, DOI 10.1017/jfm.2012.511.

[38] D. T. Squire, C. Morrill-Winter, N. Hutchins, M. P. Schultz, J. C. Klewicki, I. Marusic, Comparison of turbulent boundary layers over smooth and rough surfaces up to high Reynolds numbers, Journal of Fluid Mechanics 795 (2016) 210–240, DOI 10.1017/jfm.2016.196.

[39] H. M. Nagib, K. A. Chauhan, Variations of von Kármán coefficient in canonical flows, Physics of Fluids 20 (10) (2008) 101518, DOI 10.1063/1.3006423.

[40] K. A. Chauhan, P. A. Monkewitz, H. M. Nagib, Criteria for assessing experiments in zero pressure gradient boundary layers, Fluid Dynamics Research 41 (2) (2009) 021404, DOI 10.1088/0169-5983/41/2/021404.
[41] A. Perry, J. D. Li, Experimental support for the attached-eddy hypothesis in zero-pressure-gradient turbulent boundary layers, Journal of Fluid Mechanics 218 (1990) 405–438, DOI 10.1017/S0022112090001057.
[42] P. S. Jackson, On the displacement height in the logarithmic velocity profile, Journal of Fluid Mechanics 111 (-1) (1981) 15, DOI 10.1017/s0022112081002279.
[43] J. Loureiro, A. S. Freire, Transient thermal boundary layers over rough surfaces, International Journal of Heat and Mass Transfer 71 (2014) 217–227, DOI 10.1016/j.ijheatmasstransfer.2013.11.076.
[44] P. A. Krogstad, R. A. Antonia, L. W. B. Browne, Comparison between rough- and smooth-wall turbulent boundary layers, Journal of Fluid Mechanics 245 (-1) (1992) 599, DOI 10.1017/s0022112092000594.
[45] J. P. Bons, St and cf Augmentation for Real Turbine Roughness With Elevated Freestream Turbulence, Journal of Turbomachinery 124 (4) (2002) 632–644, DOI 10.1115/1.1505851, URL https://doi.org/10.1115/1.1505851.
[46] B. Kader, Temperature and concentration profiles in fully turbulent boundary layers, International Journal of Heat and Mass Transfer 24 (9) (1981) 1541–1544, DOI 10.1016/0017-9310(81)90220-9.
[47] A. E. Perry, P. H. Hoffmann, An experimental study of turbulent convective heat transfer from a flat plate, Journal of Fluid Mechanics 77 (2) (1976) 355–368, DOI 10.1017/s0022112076002152.
[48] I. Marusic, G. J. Kunkel, Streamwise turbulence intensity formulation for flat-plate boundary layers, Physics of Fluids 15 (8) (2003) 2461–2464, DOI 10.1063/1.1589014.
[49] P. H. Alfredsson, R. Örlü, A. Segalini, A new formulation for the streamwise turbulence intensity distribution in wall-bounded turbulent flows, European Journal of Mechanics - B/Fluids 36 (2012) 167–175, DOI 10.1016/j.euromechflu.2012.03.015.
[50] P. H. Alfredsson, R. Örlü, The diagnostic plot — a litmus test for wall bounded turbulence data, European Journal of Mechanics - B/Fluids 29 (6) (2010) 403–406, DOI 10.1016/j.euromechflu.2010.07.006.
[51] N. Hutchins, I. Marusic, Evidence of very long meandering features in the logarithmic region of turbulent boundary layers, Journal of Fluid Mechanics 579 (2007) 1–28, DOI 10.1017/s0022112006003946.
[52] R. Mathis, N. Hutchins, I. Marusic, Large-scale amplitude modulation of the small-scale structures in turbulent boundary layers, Journal of Fluid Mechanics 628 (2009) 311–337, DOI 10.1017/s0022112009006946.
[53] H. Cheng, I. P. Castro, Near-Wall Flow Development After A Step Change In Surface Roughness, Boundary-Layer Meteorology 105 (3) (2002) 411–432, DOI 10.1023/a:1020355306788.
[54] W. H. Schofield, Turbulent Shear Flows Over a Step Change in Surface Roughness, Journal of Fluids Engineering 103 (2) (1981) 344–351, DOI 10.1115/1.3241744.
[55] D. H. Wood, Internal boundary layer growth following a step change in surface roughness, Boundary-Layer Meteorology 22 (2) (1982) 241–244, DOI 10.1007/bf00118257.
[56] B. Ganapathisubramani, N. Hutchins, W. T. Hambleton, E. K. Longmire, I. Marusic, Investigation of large-scale coherence in a turbulent boundary layer using two-point correlations, Journal of Fluid Mechanics 524 (2005) 57–80, DOI 10.1017/s0022112004002277.
[57] M. M. Pimenta, R. J. Moffat, W. M. Kays, The turbulent boundary layer: an experimental study of the transport of momentum and heat with the effect of roughness, Tech. Rep. HMT-21, Stanford University, Thermosciences Division, 1975.
[58] H. Coleman, R. Moffat, W. Kays, Momentum and energy transport in the accelerated fully rough turbulent boundary layer, Tech. Rep. HMT-24, Stanford University, Thermosciences Division, 1976.
[59] R. A. Antonia, H. Q. Danh, A. Prabhu, Response of a turbulent boundary layer to a step change in surface heat flux, Journal of Fluid Mechanics 80 (1) (1977) 153–177, DOI 10.1017/s002211207700158x.
[60] J. R. Garratt, The internal boundary layer – A review, Boundary-Layer Meteorology 50 (1-4) (1990) 171–203, DOI 10.1007/bf00120524.